Annu. Rev. Nucl. Part. Sci. 2002. 52:425–69
doi: 10.1146/annurev.nucl.52.050102.090650

THE RHIC ACCELERATOR*

M. Harrison,[1] S. Peggs,[2] and T. Roser[2]
[1]*Superconducting Magnet Division,* [2]*Collider-Accelerator Department, Brookhaven National Laboratory, Upton, New York 11973; email: harrison@bnl.gov; peggs@bnl.gov; roser@bnl.gov*

Key Words polarized protons, relativistic heavy ion collider, superconducting magnets, transition crossing

PACS Codes 29.27.−a, 41.85.−p, 85.25.Ly

■ **Abstract** This review discusses the design and initial operation of the Relativistic Heavy Ion Collider (RHIC), noting the novel features of a heavy ion collider that are distinct from conventional hadron colliders. These features reflect the experimental requirements of operation with a variety of ion species over a wide energy range, including collisions between ions of unequal energies and polarized protons. Other unique aspects of RHIC include intrabeam scattering, interaction-region error compensation, and transition crossing with a slow ramp rate. The RHIC facility has just completed the second physics run after beam commissioning in 2000.

CONTENTS

1. INTRODUCTION

The primary motivation for colliding heavy ions at ultra-relativistic energies is the belief that it is possible to create macroscopic volumes of nuclear matter at temperatures and energy densities high enough to induce a phase transition from hadronic matter to a confined plasma of quarks and gluons. The main goal of the Relativistic Heavy Ion Collider (RHIC) is to provide head-on collisions at energies up to 100 GeV/u per beam for very heavy ions, namely $^{197}Au^{79}$, but the program also calls for lighter ions all the way down to protons, including polarized protons. Luminosity requirements for the heaviest ions are specified to be in the 10^{26}–10^{27} cm^{-2} s^{-1} range. The higher Au-Au total cross section results in interaction rates comparable to *p-p* colliders, although the luminosity is several orders of magnitude lower than in those machines. A short interaction point (IP) length ($\sim$20 cm rms) is desirable for optimum detector design.

A fundamental requirement of a collider is that it operate over long periods of time with the beams stored at high energies. Attaining high beam energies in an accelerator of limited physical size requires magnets capable of achieving high magnetic fields. These two basic requirements dictate the use of superconducting technology for the RHIC magnets, which minimizes power consumption while allowing much higher magnetic fields than those of conventional copper conductors and iron magnets. The penalty for adopting superconducting technology is the additional technical complexity and cost of those systems necessary to operate at a temperature of 4 K.

The heavy ion aspect of RHIC strongly influences the accelerator design. The mutual Coulomb repulsion between the beam particles (intrabeam scattering) is proportional to Z^4/A^2 and thus is much stronger for gold ions than for protons. The heavy ion beams grow within a few hours to large transverse and longitudinal dimensions. In order to accommodate physically large beams, the RHIC arc sections have stronger focusing than is typical for proton machines, with short half-cells composed of a single dipole and quadrupole assembly.

A unique feature of the physics program is the plan to collide beams of different ion species at the same energy per nucleon. In the extreme case of colliding protons on gold ions, beam rigidities differ by a factor of 2.5. This suggests a machine design based on two separate rings that can operate at two different magnetic field settings to maintain the necessary equal rotation frequencies. Because a single interaction region (IR) design cannot accommodate such different beam energies, in RHIC the beams are separated immediately downstream of the collision point before the focusing elements. To allow maximum flexibility in luminosity between the different experiments, the optics for each IR can be independently varied while maintaining a match to the arc sections.

The injection energy of 10 Gev/u into RHIC is determined by the Alternating Gradient Synchrotron (AGS) complex, and the top energy of 100 GeV/u is prescribed by the experimental program, resulting in a dynamic range of 10 to 1. As in most colliders, a short bunch length is desirable, and in RHIC a low-frequency

(28 MHz) RF system is used for capture and acceleration whereas a high-frequency (198 MHz) storage system is used for collisions.

RHIC is the first superconducting, and hence slow-ramping, accelerator to pass through transition. The machine's transition gamma (γ_T) jump minimizes problems of transition crossing. The transition energy is manipulated by a slight modification of the dispersion function through a section of each arc employing pulsed quadrupoles. Most of the arc section lattice is unaffected by the jump and thus the beam size is essentially unchanged. A second pulsed quadrupole circuit maintains the horizontal and vertical betatron tunes. (The betatron tune is the number of oscillations a particle makes in one revolution of the accelerator.)

RHIC will be by far the highest-energy polarized proton facility. The spin vector precession frequency is proportional to $G\gamma$ (where G is the anomalous magnetic moment of the proton, and γ is the Lorentz factor), so the spin tune increases along with the beam energy. This, in turn, increases the number and strength of potentially depolarizing resonances arising from both the magnetic field errors (imperfection resonances) and the quadrupole focusing fields themselves (intrinsic resonances). The higher the beam energy, the more difficult it is to maintain beam polarization. In addition, polarized proton operation requires much tighter tolerances, over the vertical closed orbit and the betatron tunes up the ramp, than regular heavy ion operation. The traditional methods of maintaining polarization, such as tune jumps and harmonic orbit corrections, would not be sufficient at RHIC, so each ring has two full Siberian snakes.

Table 1 outlines the RHIC machine parameters derived from these general requirements.

2. RHIC DESIGN AND LAYOUT

The complete RHIC facility is a complex set of accelerators interconnected by beam transfer lines. The collider, shown schematically in Figure 1, is located in the 3.8-km-circumference tunnel north of the AGS.

The collider is composed of two identical, quasicircular rings separated horizontally by 90 cm, and oriented to intersect at six locations. The collision points occur in the center of the IRs, where the beams are focused down to a small spot size and collide head-on. The IRs are spaced equidistant around the circumference, separated by arc sections. The main quadrupoles and dipoles are powered by independent electrical circuits and are cooled by a single refrigerator.

Each ring consists of three inner and three outer arcs and six insertion regions joining them. Each arc consists of 11 FODO cells, with each half-cell consisting of a single dipole and a spool-piece assembly containing a quadrupole, sextupole, and concentric correction elements. Figure 2 shows the collider layout along with the standard cell schematic.

The nominal magnetic rigidity of the dipoles is 839.5 Tm, which corresponds to a design field of 3.45 T at 100 GeV/u. Injection takes place at $\gamma = 10.25$ ($B\rho = 79.0$ Tm). The half-cell length of 15 m has beta functions in the range

TABLE 1 Major parameters for RHIC*

Parameter	Value	Units
Kinetic energy, inj.-top, Au (each beam), protons	10.8–100 28.3–250	GeV/u GeV
No. of bunches/ring	60 (120)	
Circumference	3833.845	m
Number of crossing points	6	
β^*, injection, H/V	10	m
β^*, low-beta insertion, H/V	1	m
Betatron tunes, H/V	28.19/29.18	
Magnetic rigidity, injection top energy	79.0 839.5	Tm Tm
Number of dipoles (192/ring + 12 common)	396	
Number of quadrupoles (276 arc + 216 insertion)	492	
Dipole field at 100 GeV/u, Au	3.45	T
Arc dipole effective length	9.45	m
Arc quadrupole gradient	71.2	Tm

*Definitions: β^*, interaction point beta; H/V, horizontal/vertical.

of 10.5–50 m and a beta-dispersion of 0.8–1.8 m. These relatively small values are dictated by the need to minimize the physical size of a beam (i.e., maximize the dynamic aperture and thus intensity lifetime) with relatively large emittances (40π μm normalized 95% transverse, 1.2 eV-s/u longitudinal). The dipole coil inner diameter of 8 cm is determined both by the beam size at injection and by the projected emittance growth, which occurs during a stored beam operation (a "store"), at as low an energy as 10 GeV/u. The arc quadrupoles, also having a coil inner diameter of 8 cm, operate at a maximum gradient of 72 T/m. A cross section of an arc dipole of length 9.45 m is shown in Figure 3. The magnets are conceptually similar to the HERA dipoles, with a "cold-iron" design and cryogenic transfer lines located in the cryostat.

Beams collide at the crossing point of the insertions. These regions contain the optics necessary for producing small betatron amplitude functions β^*, a zero dispersion at the crossing point, and the magnetic steering to bring the beams into head-on collisions. The "non-arc" regions also contain the warm regions where the machine utilities reside, such as injection, beam abort, RF systems, collimators, and specialized instrumentation. Locations available for these devices are the 30 m section between Q3 and Q4, the missing dipole between Q7 and Q8, and the section adjacent to the short D9 dipole. The magnetic elements in the region from Q10 to Q4 are identical in cross section, but not in length, to those in the standard cell.

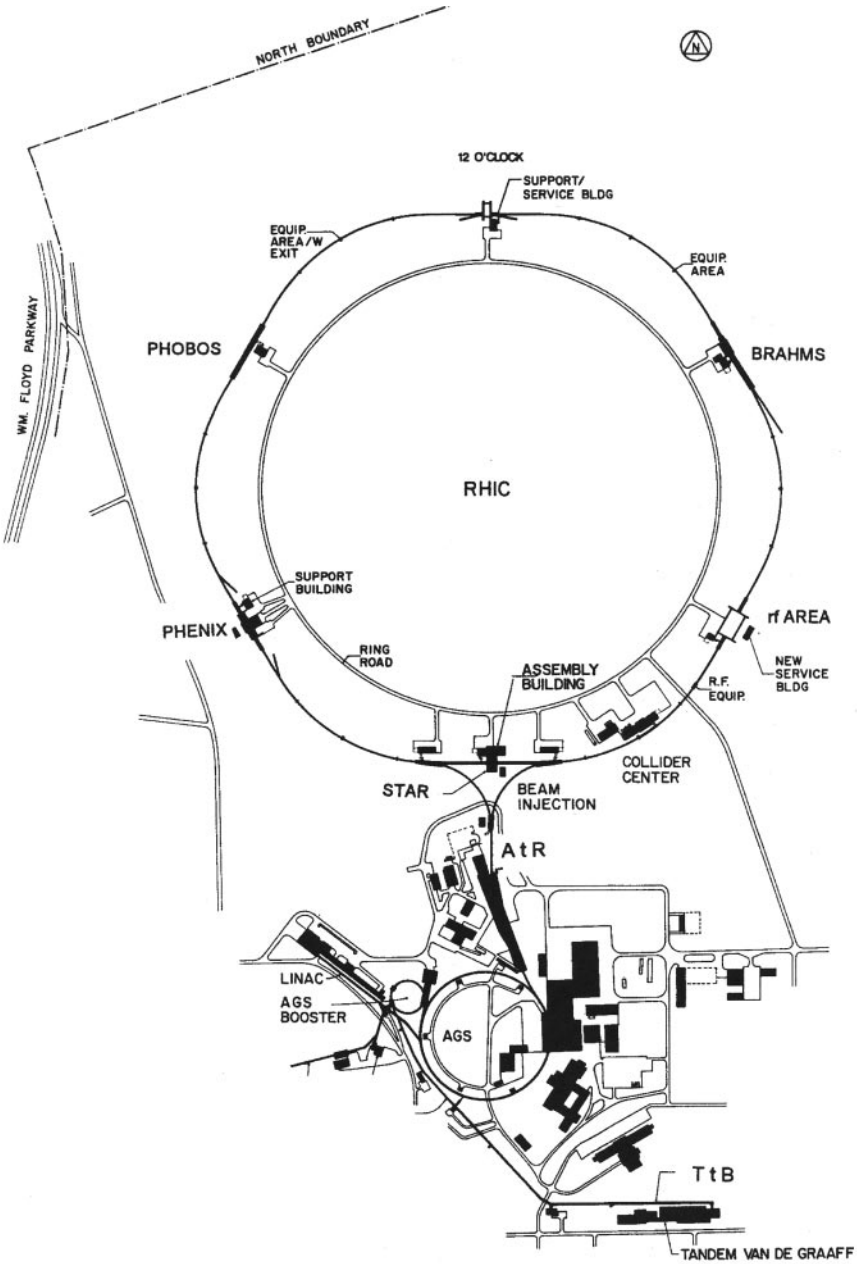

Figure 1 Overall layout of the Brookhaven National Laboratory accelerator complex, consisting of LINAC, boosters, AGS, AtR, and RHIC.

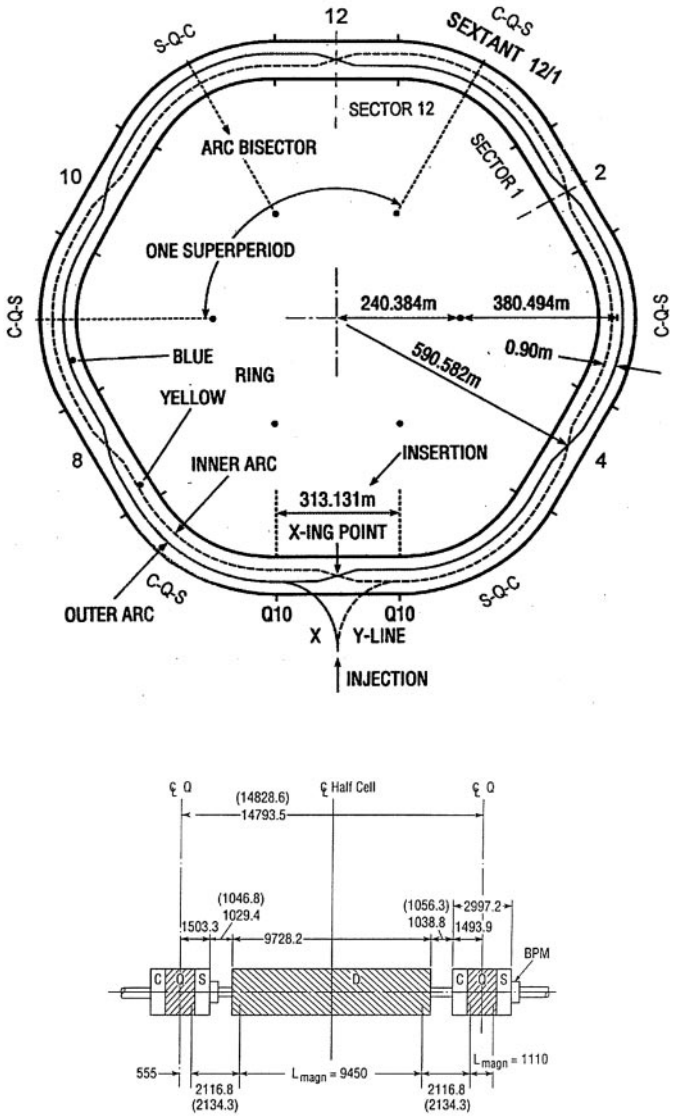

Figure 2 Collider geometric layout and arc region half-cell.

The final-focus triplet (Q1, Q2, and Q3) and bending magnets (D0 and DX) are nonstandard magnets with apertures of 13 cm, 10 cm, and 18 cm, respectively. The focusing is relaxed at injection with a β^* value of 10 m. During collisions at maximum energy, β^* 1 m can be attained, resulting in a maximum β of about 1400 m in the triplet quadrupoles. The maximum focusing strength of 48 T/m is determined by both the physical beam size in the triplet and the strength of the trim quadrupoles at Q4, Q5, and Q6. The lattice functions in the IRs are shown

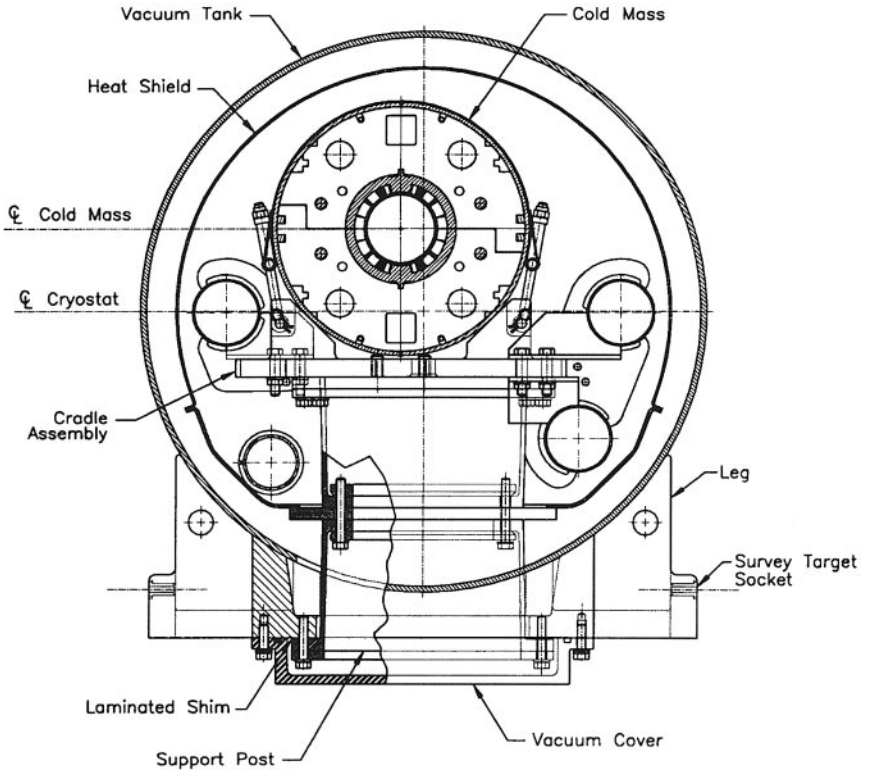

Figure 3 RHIC superconducting dipole cross section.

in Figure 4. Each insertion is independently adjustable and can be matched over a machine tune range of ± 1 unit. The phase advance across the insertion is almost constant during the squeeze (when β^* is reduced from 10 m to 1 m), as is the triplet excitation.

3. SUPERCONDUCTING MAGNET SYSTEM

The ring magnets naturally fall into two types (Table 2): the 8-cm-aperture elements that are used throughout the arc regions and constitute the majority of the magnets, and the less common variable-aperture magnets used in the immediate vicinity of the IP.

The 8 cm dipoles, quadrupoles, and sextupoles were all produced by industry. The low-current correctors, final-focus triplet quadrupoles, and beam-splitting dipoles were produced at Brookhaven National Laboratory. Brookhaven also integrated the quadrupoles, sextupoles, and correctors into a single cryogenic module. The dipole magnets, produced by the Northrop-Grumman Corporation in a

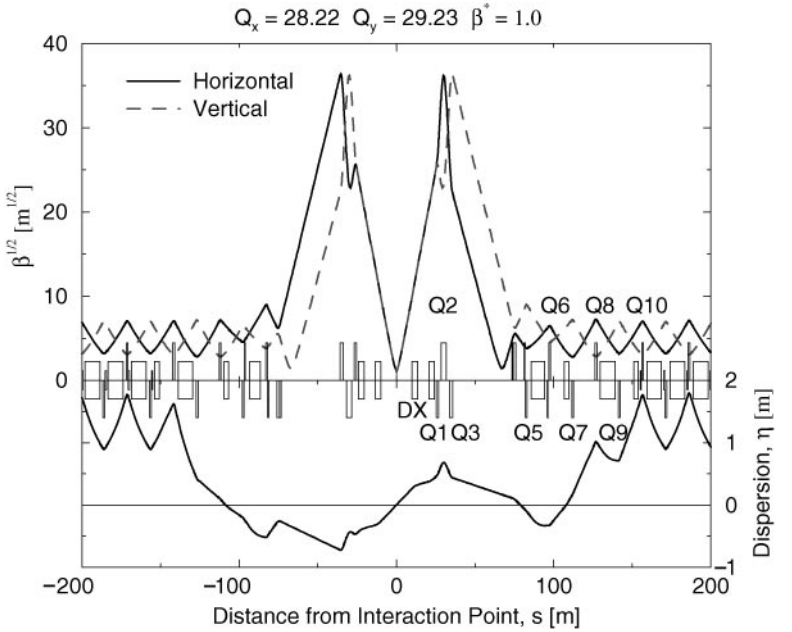

Figure 4 Lattice functions in the interaction regions for collision optics.

TABLE 2 RHIC magnet inventory

Magnet	Number	Aperture, mm	Length, m
Dipoles			
Arc	264	80	9.45
D5I, D5O	12, 12	80	6.92, 8.71
D6, D8, D9	24, 24, 24	80	2.95, 9.45, 2.95
D0	24	100	3.6
DX	12	180	3.7
Quadrupoles			
Arc	276	80	1.13
Q4, Q5, Q6	24, 24, 24	80	1.83, 1.13, 1.13
Q7, Q8, Q9	24, 24, 24	80	0.95, 1.13, 1.13
Q1, Q2, Q3	24, 24, 24	130	1.44, 3.40, 2.10
Sextupoles			
Arc, Q9	276, 12	80	0.75
Trim Quads			
Q4, Q5, Q6	24, 24, 24	80	0.75
Correctors			
B, C, D, E, F	96, 132, 78, 78, 36	80	0.5
I, J, K, L, M	12, 12, 24, 12, 12	130	0.5

build-to-print contract, were complete cryogenic elements suitable for immediate installation.

The crucial aspects of superconducting accelerator magnets are field quality and quench threshold. Except for the 10% of the arc magnets that were produced first, cold testing was limited to one magnet in ten, since it was deemed unfeasible to test each magnet. Field quality was primarily measured at room temperature. It therefore became important to establish a good correlation between warm and cold magnetic field measurements at the 10^{-5} level. An analysis of the complete data set demonstrated good warm/cold field correlations at this accuracy after compensating for yoke saturation effects. Figure 5 shows a plot of the warm/cold correlation for the decapole harmonic of the arc dipoles. The agreement is good to the desired accuracy for this and the other field harmonics.

The magnet set demonstrates excellent field quality with very small random multipole field components by virtue of tight mechanical tolerances on the cable dimensions. The systematic component of the field harmonics is optimized for low-field performance at injection, with yoke saturation apparent in the allowed harmonics at high field. During collisions, the dynamic aperture is determined by the triplet quadrupoles. Figure 6*a* shows the quench performance of the 8 cm dipole magnets with the minimum and plateau quench currents for a set of 60 magnets.

Because only 20% of the arc magnets were measured cold, it was important to demonstrate sufficient operating margin to justify limited testing. None of the

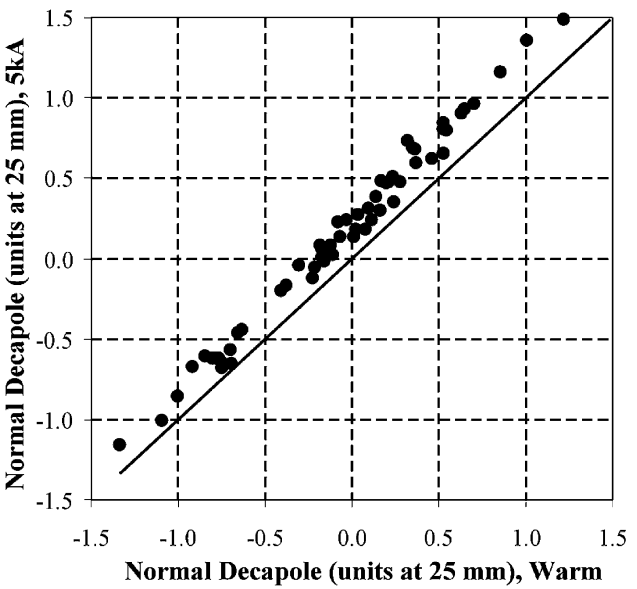

Figure 5 Warm/cold correlation for the decapole harmonic of the arc dipoles. The "units" are 1 part in 10,000 at 25 mm from the center of the magnet.

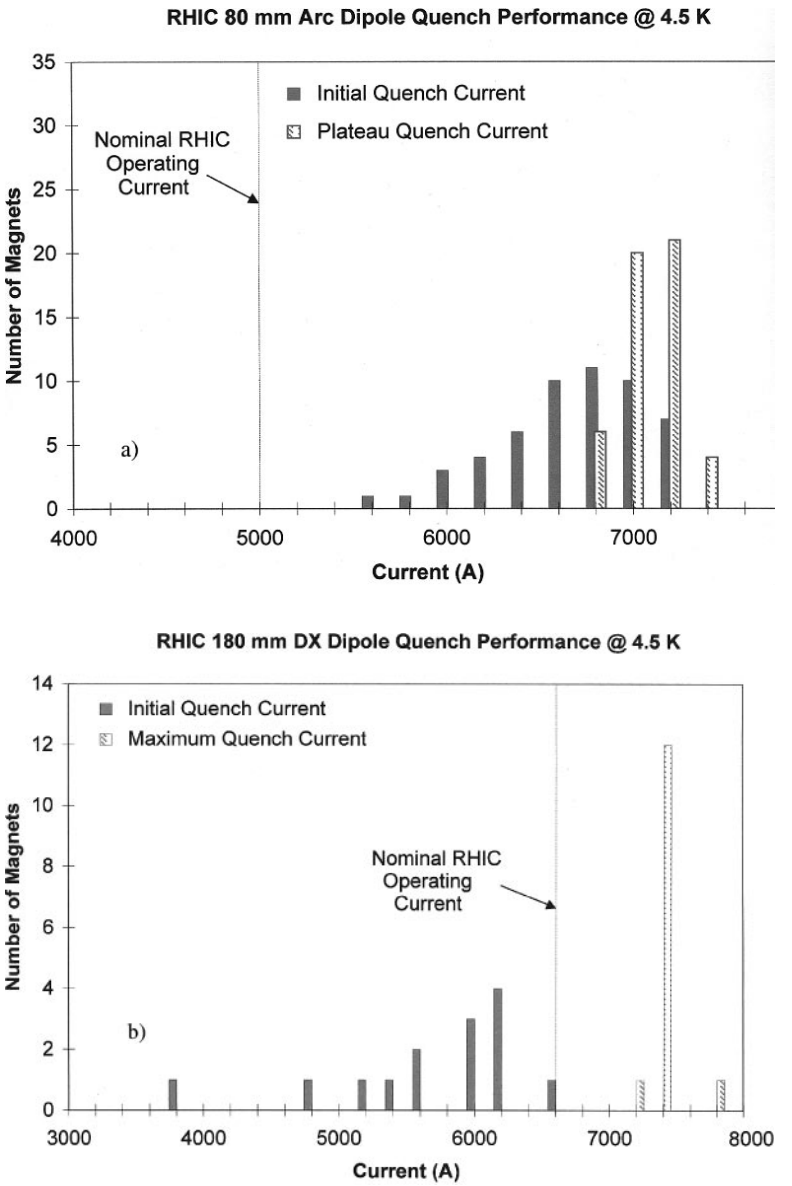

Figure 6 Quench performance for (*a*) arc dipoles and (*b*) beam-separation dipoles.

magnets tested had an initial quench current less than the nominal operating level. The plateau quench level demonstrates a healthy 30% operating margin. The situation of the IR magnets, however, was not so pristine. The large-aperture dipole magnets did indeed have an initial quench threshold below the nominal operating point of 6 kA. The plateau level for these elements had only a $\simeq$10% operating margin and did show some loss of training on a thermal cycle. (Figure 6*b* shows the data on these magnets.) Consequently, they were all cold tested prior to installation in the ring.

The magnet performance during the commissioning phase was well predicted by these measurements. There were no magnet failures during turn-on, demonstrating that the warm measurements were indeed sufficient to guarantee magnet fidelity. During the first ramps to full energy only the large-aperture dipole showed any training quenches, and top energy was reached after seven quenches. After three running periods, no spontaneous arc magnet quenches have been observed.

4. INTRABEAM SCATTERING

Intrabeam scattering (IBS) is Coulomb scattering between particles within a bunch. Assuming that the particle distribution remains Gaussian in the six-dimensional phase space, various theoretical treatments (1, 2) describe the time evolution of the bunch size. Because the horizontal closed orbit is correlated to momentum, the growth rates change dramatically depending on whether accelerator energy is above or below transition. Because RHIC stores the beams for long periods at high energy, the behavior above transition is critical. In this case, the beam emittance increases in all planes.

The evolution of the root mean squared (rms) beam size σ due to IBS for a bunched beam can be described by (3)

$$\begin{bmatrix} \frac{1}{\sigma_x}\frac{d\sigma_x}{dt} \\ \frac{1}{\sigma_y}\frac{d\sigma_y}{dt} \\ \frac{1}{\sigma_p}\frac{d\sigma_p}{dt} \end{bmatrix} = \frac{Z^4 N_b}{A^2} \frac{r_0^2 L_c (\beta c)}{8\pi(\beta\gamma)^4 \epsilon_x \epsilon_y \epsilon_s} F(\chi) \begin{bmatrix} -a^2/2 + d^2 \\ -b^2/2 \\ 1 - d^2 \end{bmatrix}, \qquad 1.$$

where N_b is the number of particles per bunch, L_c is a form factor of $\sim$20, r_0 is the classical radius of the ion, and Z and A are atomic number and atomic weight. Neglecting the (presumably small) effect of vertical dispersion, one has

$$d = \frac{y_x \sigma_p}{\sqrt{\sigma_x^2 + D_x^2 \sigma_p^2}}$$

$$a = \frac{\beta_x d}{y_x \gamma} \qquad 2.$$

$$b = \frac{\beta_y \sigma_x}{\beta_x \sigma_y}\, a$$

$$\chi = \frac{a^2 + b^2}{2}. \qquad 3.$$

The function $F(\chi)$ is defined by

$$F(\chi) = \frac{(1 + 2\chi)I(\chi) - 3}{1 - \chi} \qquad 4.$$

with

$$I(\chi) = \frac{1}{\sqrt{\chi(\chi - 1)}} \operatorname{arth} \sqrt{\frac{\chi - 1}{\chi}} \quad (\chi \geq 1) \qquad 5.$$

$$= \frac{1}{\sqrt{\chi(1 - \chi)}} \arctan \sqrt{\frac{1 - \chi}{\chi}} \quad (\chi < 1). \qquad 6.$$

For high energies the growth rates are essentially independent of energy, but for RHIC the most important feature is the Z^4/A^2 dependence. The nominal gold ion bunch intensity of 10^9 particles is thus predicted to experience beam growth rates an order of magnitude greater that those of a nominal proton bunch of 10^{11} particles. Rapid beam growth results initially in a short luminosity lifetime and eventually causes beam loss when the beam becomes broader than the transverse aperture or longer than the RF bucket.

Because the projected initial luminosity lifetime for a 10^9 bunch of gold ions is only several hours, it was desirable to measure the effect of IBS during the initial RHIC operation even though the bunch intensities were below the design value, only $\simeq 2.5 \times 10^8$.

The longitudinal emittance and bunch area were calculated from measurements of the bunch length from a wall-current monitor (4) together with the known RF parameters. The bunch lengths were measured at 4 s intervals with a resolution of 0.25 ns. Each bunch profile was then fitted to a Gaussian distribution. The results of this fit are shown in Figure 7 for 314 bunches as a function of store time.

Growth times are taken from the derivative of such bunch length curves after they are fitted to a fifth-order polynomial. Figure 8 shows the initial longitudinal growth times. The data show a long tail, some bunches with very short lifetimes, and a relatively broad peak with an average value of $\sim$2 h. This agrees quite well with the computed value of 1.8 ± 1.0 h obtained by numerically integrating the IBS equations with the appropriate initial bunch parameters.

During the initial operation of RHIC, the most accurate transverse emittance measurements during collisions were made by Vernier scans at the IP. This involves local orbit bumps across the IR to scan the beams in small transverse steps (200 μm) while measuring the collision rate as a function of the relative beam separation. From these data the effective size of the beam at the IP is calculated. Since this method cannot distinguish between the two beams, equal beam sizes are assumed. The results of these measurements are given in Figure 9, which shows the transverse emittance evolution for gold ions in both planes during a high-energy beam store.

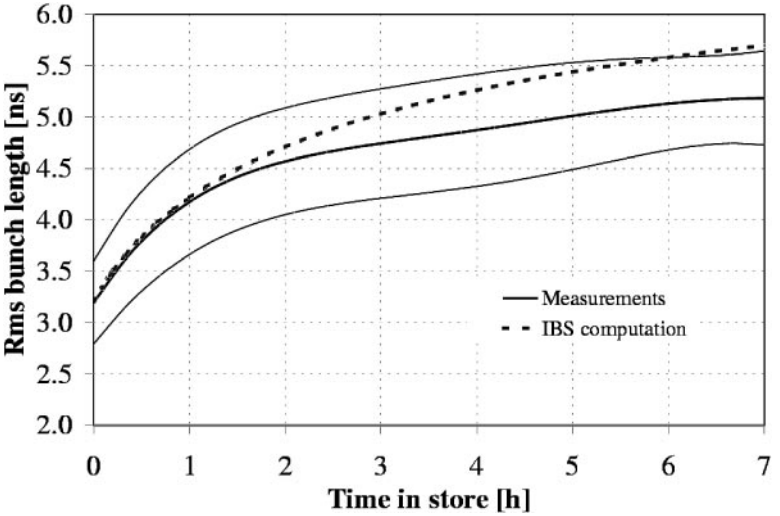

Figure 7 Bunch length evolution compared with the predicted IBS value. The central line shows the average value, the others are $\pm 1\,\sigma$.

Unlike the longitudinal plane, the results show an emittance growth rate much larger than that expected from IBS, as well as a discrepancy between horizontal and vertical measurements. There are several possible reasons for these findings: Power-supply noise would influence the growth rate and could cause more horizontal growth than vertical, the beam-beam interaction at the collision points would increase transverse growth rates, and during the run small horizontal

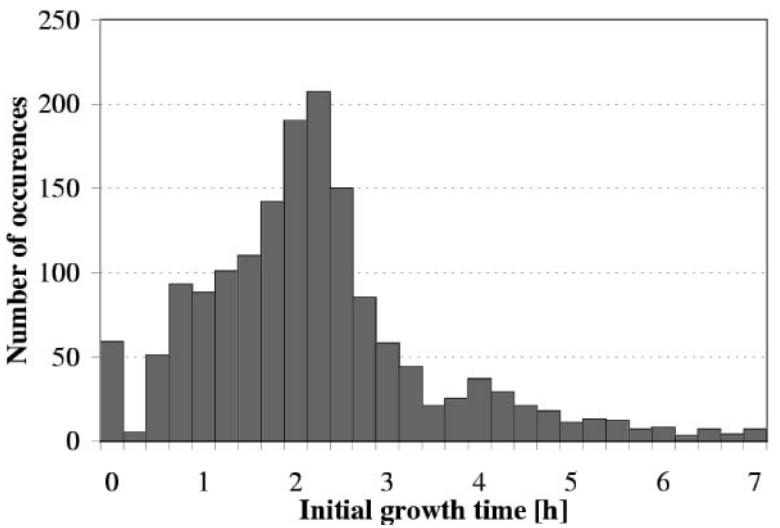

Figure 8 The initial growth time of 1719 bunches in the Blue ring.

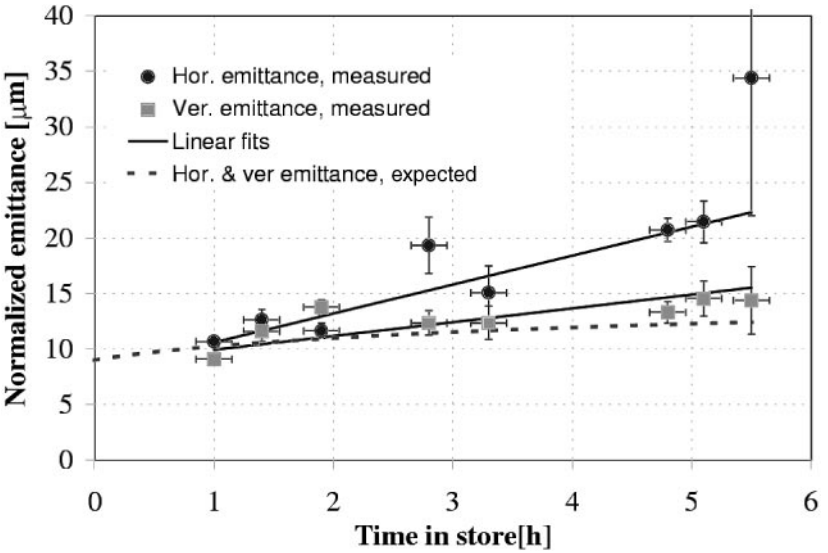

Figure 9 Transverse emittance measurements as a function of time from the start of the beam store.

oscillations were detected in the final-focus quadrupoles related to the cryogenic system. Reference (5) provides a more complete description of the beam lifetime measurements.

Because these measurements were made during the early operation of the machine, it is not too surprising that the measured transverse beam growth rates are larger than those calculated from IBS. A better test will be possible when results from operations with protons, or some other ion species, become available. This will permit the effect of other emittance growth mechanisms to be untangled from the more fundamental IBS process. Indeed, RHIC's ability to operate with several different beam particle species at high energies should allow the most accurate IBS measurements in any large accelerator.

5. MAGNETIC OPTICS

One unique feature of the RHIC magnetic optics is its ability to collide ions of different mass and charge—for example, deuterons on gold or protons on gold—in addition to more conventional collisions between similar species, such as gold on gold or polarized protons on polarized protons (6). Figures 1 and 2 show RHIC's composition of six arcs joined by six relatively straight IRs. At the center of each IR is an IP. One function of the IR optics is to bring the two counter-rotating beams—similar or dissimilar—from separate beam pipes into a common beam pipe, so that they collide head-on at the IP.

Another (more conventional) function of the IR optics is to make the round beam size σ^* at the IP as small as possible, in order to make the luminosity L as large as possible, since

$$L = \frac{MN^2 f_R}{4\pi\sigma^{*2}}, \qquad 7.$$

where M bunches of N ions collide with a revolution frequency of f_R. In general, the rms beam size is given by

$$\sigma = \sqrt{\frac{\epsilon\beta}{6\pi(\beta\gamma)} + \left(\eta\frac{\sigma_p}{p}\right)^2}, \qquad 8.$$

where ϵ is the 95% normalized transverse emittance, β is the beta function, $\beta\ \gamma$ is the Lorentz-relativistic factor, σ_p/p is the rms relative momentum spread, and η is the dispersion function. Thus, two design goals of the IR optics are to reduce the IP dispersion function η^* to zero and to make the beta function β^* as small as possible.

A second unique feature of the RHIC optics is its ability to perform a first-order matched transition jump. All ion species except for protons cross transition during acceleration in RHIC, which is the first superconducting accelerator to face this challenge. Transition occurs when the differential of circulation time with respect to $\delta = \Delta p/p_0$, the off-momentum parameter, is zero. This happens when the Lorentz γ of the synchronous particle (with $\delta = 0$) accelerates through the transition value γ_T, which has a nominal value of 22.89 in RHIC. The transition gamma is a property of the lattice, and so it is possible to intervene to quickly drop γ_T through γ, rather than waiting for γ to slowly accelerate through γ_T. This is done by manipulating the dispersion function η in the arcs.

These three functions of the magnetic optics—beam separation, beam size squeezing, and a first-order transition jump—are described in more detail below.

5.1. Beam Separation

Figure 10 shows how the DX and D0 dipoles separate the beams into two beam pipes before they enter the Q1, Q2, and Q3 quadrupoles that comprise the IR triplet. The principal advantage of separating the beams immediately, before the first quadrupole, is the ability to collide dissimilar ion beams. This is because the Blue and Yellow ring triplets must be independently set to different gradient strengths when dissimilar beams have dissimilar rigidities.

Beam-beam collisions are synchronously locked to the IP by ensuring that the revolution periods of the two beams are identical. The nominal way to do this is to circulate the two beams with the same Lorentz speed β, while ensuring that each beam travels (on average) down the center of the beam pipe, so that the two circumferences are also identical. This synchronization leads to two different

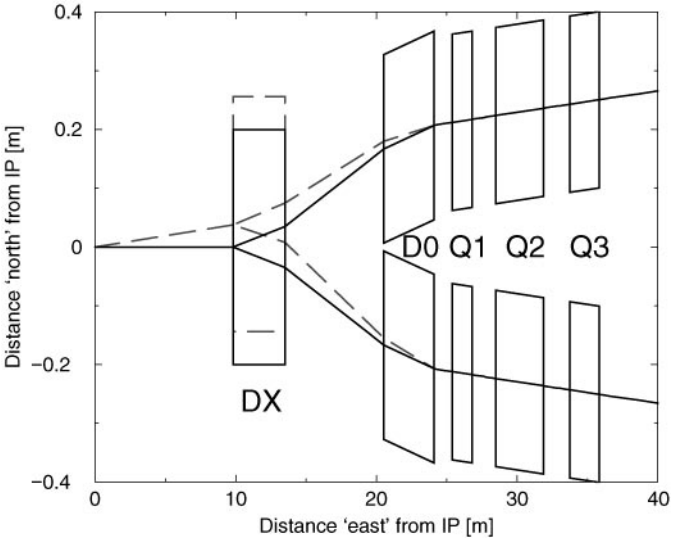

Figure 10 Beam separation close to the interaction point. The dashed lines show the translation of the DX magnet that must occur in the most extreme example of dissimilar species—protons on gold.

rigidities $B\rho$ when dissimilar species are colliding, since

$$B\rho[\mathrm{Tm}] = 3.3356\frac{AM_0}{Z}\beta\gamma, \qquad 9.$$

where M_0 is the mass per nucleon in GeV/c^2. For example,

$$(B\rho)_{\mathrm{Au}} = 7.7450\ \beta\gamma, \qquad 10.$$

$$(B\rho)_d = 6.2564\ \beta\gamma, \qquad 11.$$

$$(B\rho)_p = 3.1297\ \beta\gamma \qquad 12.$$

for gold ions, deuterons, and protons, respectively. Table 3 shows the rigidity of the second beam when the ring containing the gold beam is fully excited, with a maximum rigidity of $B\rho = 839.5$ Tm.

Unfortunately, two beams with dissimilar rigidities must pass through a common DX dipole magnet before passing through separately adjustable D0 dipoles (dashed lines in Figure 10). Because the proton beam is bent much more than the gold beam, it is necessary to accept a common closed orbit angle of 3.8 mrad at the IP, in order for the two beams to collide head-on. This in turn makes it necessary to move the DX magnet sideways, a cumbersome and time-consuming process, in order to avoid beam scraping.

In principle, synchronous collisions of dissimilar species can also be maintained with beams of equal (and therefore maximal) rigidity by introducing a slight

TABLE 3 Parameters for equal-speed protons or deuterons, when the ring containing the gold ions is at its maximum excitation

Parameter	Value	Units
Gold rigidity, $(B\rho)_{\mathrm{Au}}$	839.5	Tm
Deuteron rigidity, $(B\rho)_d$	678.1	Tm
Proton rigidity, $(B\rho)_p$	339.2	Tm
Speed shortfall, $1-\beta$	4.3×10^{-5}	

difference in circumferences that compensates for the slight difference in speeds, $\Delta\beta$ (7). This is done by simply locking the RF frequencies of the two rings to a common value that forces the average closed orbit in each ring to move systematically inward or outward. The systematic radial shift is as much as

$$\hat{X} \approx \pm\hat{\eta}\,\frac{\Delta\beta}{2}\,\gamma_T^2\,, \qquad 13.$$

where $\hat{\eta} = 1.9$ m is the maximum dispersion in the arcs and $\gamma_T = 22.89$. This mode of operation is marginally practical for deuterons, with $\Delta\beta = 2.8\times10^{-5}$ and $\hat{X} \approx \pm7.5$ mm. There are some practical advantages in compromising between equal speed and equal rigidity operation. For example, when operation with dissimilar species will first take place, with deuteron and gold ions, it is likely that injection will take place at equal rigidities but that the collisions will occur after energy ramping to equal speeds. With unsynchronized beams at injection, the closed orbits will always remain near the center of each beam pipe.

A secondary advantage of early beam separation is the complete absence of parasitic beam-beam collisions (8). The beam-beam parameter is

$$\xi = \frac{3Nr}{2\epsilon}, \qquad 14.$$

where the classical radius r is 1.5347×10^{-18} m for protons and 48.992×10^{-18} m for gold ions, and N is the number of ions in a single bunch. Thus, the nominal gold and proton beam-beam parameters in RHIC are

$$\xi_{Au} = 0.00117\frac{N}{10^9}\frac{20\pi\ [\mu\mathrm{m}]}{\epsilon} \qquad 15.$$

$$\xi_p = 0.00366\frac{N}{10^{11}}\frac{20\pi\ [\mu\mathrm{m}]}{\epsilon}. \qquad 16.$$

For comparison, strong beam-beam effects are noticed in proton colliders when $\xi = 0.004$, with six head-on collisions per turn (9). RHIC nominally operates with 60 bunches, equally spaced (3 bunches unfilled to provide an abort gap), but operation with 120-bunch spacing is feasible. With 120 bunches, the first parasitic collision would occur 15.98 m from the IP, except that the beams enter two separate

beam pipes 15.70 m from the IP. Thus, even for 120 bunches there are no parasitic collisions in normal synchronized operation.

5.2. Interaction Region

Figure 11 shows one side of an IR, out to the first of the repetitive FODO cells in the arc. Figure 11*a* shows the magnet footprint geometry and the beam separation; Figure 11*b* shows the evolution of β and η, the optical functions. The main design goals are to make the IP dispersion function (η^*) zero and to make the beta function (β^*) small, in order to achieve the smallest possible spot at the IP. For example, if $\epsilon = 12\pi\ \mu$m, $\beta^* = 1.0$ m, and $\beta\gamma = 108.4$, then $\sigma^* = 0.13$ mm, according to Equation 8. All of the quadrupoles from Q1 to Q9 are independently adjustable in strength, and they control the evolution of the beta functions through the differential equation

$$\frac{d^2b}{ds^2} + Kb - b^{-3} = 0, \qquad 17.$$

where $b \equiv \sqrt{\beta}$ and $K(s)$ is the quadrupole strength (with a different sign in different planes). The simple solution

$$\beta(s) = \beta^* + \frac{s^2}{\beta^*}, \qquad 18.$$

valid between the IP and the first quadrupole, shows that the price of squeezing the beam size at the IP is a rapidly diverging large beam at Q1.

It is the job of the telescope to match these rapidly growing beta functions to values more typical of the arc. The (Q1, Q2, Q3) triplet transforms rapidly diverging beta functions at its entrance into rapidly converging functions at its exit. The last quadrupole in the telescope, Q4, completes this task by permitting no significant secondary beta peaks in the rest of the IR.

Quadrupoles in the dispersion suppressor module, from Q5 to Q10, have the same spacings as in the arc. However, there are missing dipoles and short dipoles between quads in the dispersion suppressor, whereas there is always one full-length dipole between neighboring quadrupoles in the arc. These missing and short dipoles modify the evolution of the dispersion function η according to the

Figure 11 Modular design of the RHIC interaction region. *Top*: Geometrical footprint of the Blue and Yellow rings, as they are separated into inner and outer arcs. The boxes show the approximate actual size of the magnets. *Bottom*: Optical behavior of the beta and dispersion functions through the telescope and dipersion suppressor modules. Dipoles are shown as rectangles centered on the horizontal axis, and quadrupoles are shown as rectangles completely above or below the axis, for horizontally focusing or defocusing quadrupoles, respectively.

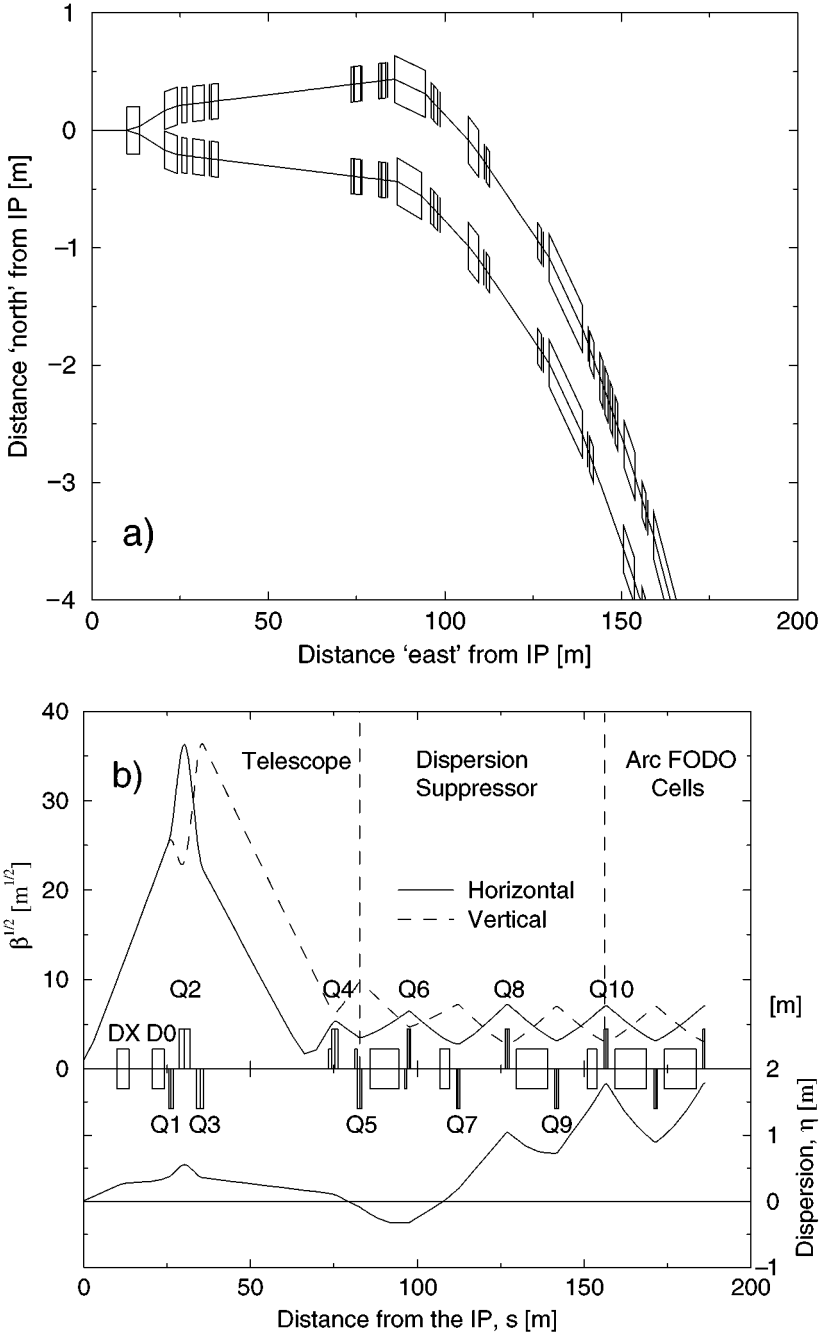

differential equation

$$\frac{d^2\eta}{ds^2} + K\eta = G, \qquad 19.$$

where the dipole bending strength $G(s) = 1/\rho$ is the inverse of the local bending radius. In this way, the dispersion suppressor matches the dispersion from $\eta \approx 0$ at the end of the telescope to the natural periodic values in the repetitive arc cells. Various specialized items, such as injection kickers and Lambertson septum magnets, are located in place of the missing dipoles.

5.3. Transition Crossing

Gold beams in RHIC accelerate with a nominal constant rate of $\gamma' \equiv d\gamma/dt \approx 1.0\ \mathrm{s}^{-1}$ over most of the energy ramp. Simulations predict that 70% of the nominal gold ion beam will be lost, and the longitudinal emittance will grow by 60%, if nothing is done to speed up transition crossing (10–14). RHIC uses a first-order matched transition jump, so that the transition energy γ_T decreases very quickly across the γ of the accelerating beam, with little beam disturbance (15, 16). "First-order" here means that the change in γ_T is proportional to the perturbation of special quadrupole corrector circuits. "Matched" means that the quadrupole arrangement minimizes optical distortions. Crucially, the high quality of matching that can be achieved in a first-order transition jump is demonstrated by the fact that the maximum dispersion during the jump is only 2.30 m, comparable to the unperturbed value of 1.84 m.

Two time scales characterize transition crossing, in the absence of a jump. The nonadiabatic time (T_C) is given by

$$T_C = \left(\frac{AE_T}{ZeV|\cos(\phi_s)|} \cdot \frac{\gamma_T^3}{h\gamma'} \cdot \frac{C^2}{4\pi c^2} \right)^{1/3}, \qquad 20.$$

with a nominal value of 0.043 s (see Table 4 for the identification and nominal values of the parameters in this equation). This is the time during which the longitudinal motion of the synchronous particle is not well represented by a slowly varying Hamiltonian (17). The other characteristic time scale, the nonlinear time (T_{NL}), is

$$T_{\mathrm{NL}} = \left(\alpha_1 + \frac{3}{2}\beta_T^2 \right) \frac{\gamma_T}{\gamma'} \delta_{\mathrm{MAX}} \qquad 21.$$

with a nominal value of 0.190 s in a $\beta^* = 10$ m lattice. This parameterizes the Johnsen effect, in which particles cross transition at different times according to their momentum offsets, with a maximum delay or advance of $\pm T_{\mathrm{NL}}$ for a particle with $\delta = \pm\delta_{\mathrm{MAX}}$, at the edge of the momentum distribution of the beam (18, 19). The nonlinear parameter α_1 varies with the lattice β^* and with the chromaticity. This is discussed in more detail below.

The nonlinear time in RHIC is much longer than the nonadiabatic time, mainly because γ' is relatively small. Without a jump, some part of the momentum

TABLE 4 Nominal RHIC transition jump parameters for gold ions

Parameter	Value	Units
Nonadiabatic time T_C	0.043	s
Nonlinear time $T_{\rm NL}$	0.190	s
Transition gamma γ_T	22.89	
Transition jump step $\Delta\gamma_T$	-0.8	
Transition jump time ΔT	0.050	s
Acceleration rate γ'	1.0	s^{-1}
Jump rate $d\gamma_T/dt$	-16.0	s^{-1}
Max. off-momentum parameter $\delta_{\rm MAX}$	0.0043	
Circumference C	3.834	km
Atomic number Z	79	
Atomic weight A	196.97	
Ions per bunch N	10^9	
Transition energy per nucleon E_T	21.4	GeV
Peak RF voltage V	0.3	MV
Stable phase ϕ_s	0.16	radians
Harmonic number h	360	
Longitudinal emittance (95%) ϵ	0.3	eV-s/u
Nonlinear parameter α_1 ($\beta^* = 10$ m)	0.43	

distribution is crossing transition at all times such that

$$|\gamma_T - \gamma| < \gamma' T_{NL} \approx 0.2. \qquad 22.$$

Thus, the RHIC transition jump should be big enough so that, including a safety factor of two,

$$|\gamma_T - \gamma| > 0.4, \qquad 23.$$

except for a very short period of time. This criterion is met by the nominal transition jump of $\Delta\gamma_T = -0.8$ in about 50 ms, as illustrated in Figure 12. Transition is crossed at about $d\gamma_T/dt \approx -16\ s^{-1}$, about 15 times faster than without a jump. Simulations performed under these conditions predict no particle loss and a longitudinal emittance increase of only about 10% (14).

5.3.1. TWO QUADRUPOLE JUMP FAMILIES The transition gamma is a property of the linear lattice given by

$$\frac{1}{\gamma_T^2} = \frac{2\pi}{C}\langle\eta\rangle = \frac{\oint \eta\, d\theta}{C}, \qquad 24.$$

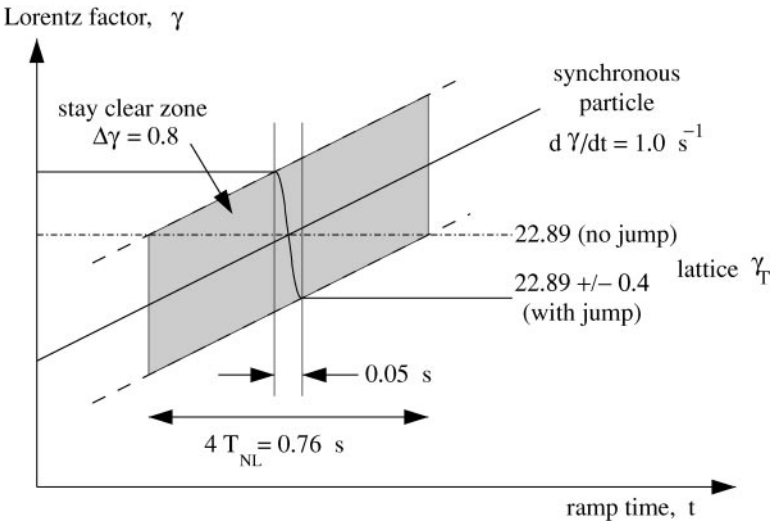

Figure 12 Schematic representation of the RHIC transition jump. Transition is crossed about 15 times faster with the jump than without.

where C is the circumference and $\langle\eta\rangle$ is the dispersion, averaged over the bending angle θ. When a set of (thin) quadrupoles labeled i is perturbed by strength q_i, the horizontal tune shifts to first order by

$$\Delta Q_H = \frac{1}{4\pi} \sum_i q_i \ \beta_{Hi}. \qquad 25.$$

The horizontal beta function at a general location with phase ϕ is perturbed by

$$\frac{\Delta\beta_H}{\beta_H} = \frac{1}{2 \ \sin(2\pi Q)} \sum_i q_i \beta_{Hi} \ \cos(2|\phi - \phi_i| - 2\pi Q), \qquad 26.$$

and similarly, the dispersion function is perturbed by

$$\frac{\Delta\eta}{\sqrt{\beta_H}} = \frac{1}{2 \ \sin(\pi Q)} \sum_i q_i \eta_i \sqrt{\beta_{Hi}} \ \cos(|\phi - \phi_i| - \pi Q). \qquad 27.$$

The phase of the perturbed beta wave propagates twice as fast as that of the dispersion wave. Thus, if two quadrupoles with identical β and η values spaced by 90° in phase are perturbed by the same amount, then the beta function is only locally perturbed between them, whereas the dispersion wave propagates globally. Similarly, if four quadrupoles spaced by 90° are identically perturbed, then both the beta and dispersion waves are locally confined (to first order).

Dispersion perturbations, whether local or global, lead directly to a change in γ_T (see Equation 24). Risselada has derived an elegant and powerful relation, valid to all orders in perturbation strength, between the change in γ_T and the values of

the dispersion function at the transition jump quadrupoles (20). It states that

$$\Delta\frac{1}{\gamma_T^2} = -\frac{1}{C}\sum_i q_i\tilde{\eta}_i\eta_i, \qquad 28.$$

where $\tilde{\eta} = \eta + \Delta\eta$ is the perturbed dispersion function. To first order in q_i, then,

$$\Delta\gamma_T = \frac{\gamma_T^3}{2C}\sum_i q_i\eta_i^2. \qquad 29.$$

This equation shows that localizing the dispersion wave does not reduce the effect on $\Delta\gamma_T$, so long as the quadrupole perturbations q_i all have the same sign. Matched first-order transition jump schemes are as efficient as unmatched first-order schemes.

Figure 13 shows the two quadrupole jump families in RHIC, in one of the six sextants. The *G* family consists of four quadrupole correctors at arc locations next to horizontally focusing quadrupoles where the design values of η, β_H, and β_V are all identical. This family has a strong effect on γ_T and also on the horizontal tune, according to Equations 25 and 29. The *Q* family consists of two pairs of quadrupole correctors. Each pair is next to focusing quads in the IR where the dispersion is almost zero, but where β_H and β_V are still close to their periodic matched arc-cell values. This second family is used to compensate the horizontal tune shift (and to suppress the much smaller vertical tune shift), with only a minor effect on γ_T. The two families are opposite, but almost equal, in strength.

Unmatched second-order transition jump schemes implemented at other accelerators have only one family of quadrupoles, usually with the same periodic value for β_i and η_i at all quads. Excessive tune shifts are usually avoided by regularly flipping the sign of the perturbation q_i, so that the first-order sums in Equations 25 and 29 are zero (21, 22). In all cases, second-order schemes incur large changes in the dispersion function, since for them

$$\Delta\gamma_T = \frac{\gamma_T^3}{2C}\sum_i q_i\Delta\eta_i\eta_i, \qquad 30.$$

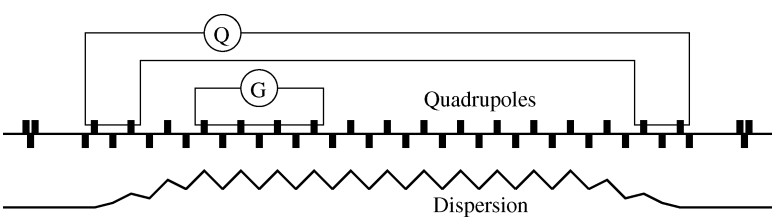

Figure 13 Schematic of the two quadrupole jump families in one of the six RHIC sextants. The dispersion is nonzero, but small, at some quads in the *Q* family.

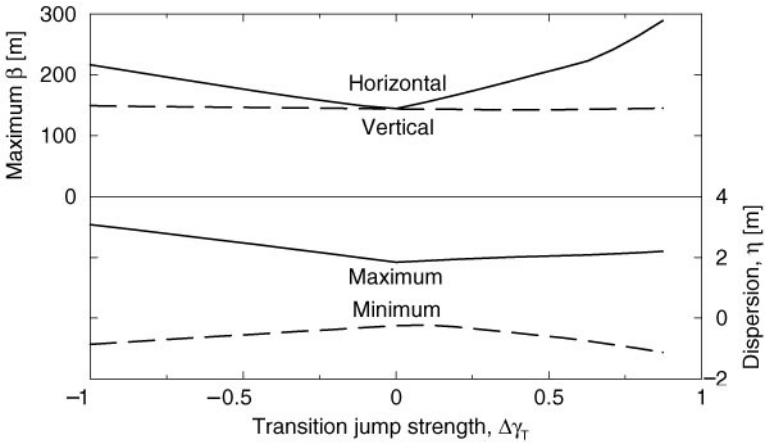

Figure 14 Global maximum beta functions, and maximum and minimum dispersions, as a function of the transition shift $\Delta\gamma_T$ in a RHIC lattice with $\beta^* = 10$ m at each IP. The fixed ratio of the two quadrupole jump families has been optimized for a jump with $\Delta\gamma_T = \pm 0.4$.

where $\Delta\eta_i$ (which remains first-order in q_i) must be large. Thus, the change in γ_T is second-order in perturbation strength, and the β and dispersion variations are large and global. Second-order schemes lead to intrinsically large beams at transition, a major disadvantage (23).

Figure 14 shows how the global extrema of the beta functions and the dispersion depend on the transition shift $\Delta\gamma_T$, over a range that corresponds to extreme power-supply currents of ± 50 A (16, 24). Even though the phase advance between quadrupole correctors is significantly less than 90° and some optical distortions are present, the level of perturbation wave localization is still quite high. The matching is very good over a wide range, even well beyond the nominal values of $\Delta\gamma_T = \pm 0.4$. In particular, the maximum value of $|\eta|$ changes only slightly and does not compound the difficulty of σ_p/p becoming very large near transition. Figure 15 shows the corresponding variation of the fractional tunes from $\Delta\gamma_T = -0.5$ to $\Delta\gamma_T = +0.5$. These tune shifts are readily measured, in practice, by DC excitation of the quadrupole families.

According to Equation 21, it is also possible to fight transition by moving the nonlinear parameter closer to its ideal value of $\alpha_1 = -1.5$, so that ions of all momenta cross transition in unison (16, 25). Figure 16 shows how α_1 changes with the β^* of the RHIC lattice and with the chromaticities ($\frac{dQ}{d/\delta}$), assumed equal. From this perspective alone, it is best to pass through transition in a lattice with $\beta^* = 3$ m at each IP. However, such a small value of β^* makes the beam uncomfortably large in the triplet, according to Equations 8 and 18, when the relatively small value of $\beta\gamma \approx 23$ is taken into account. Also, the tune variation

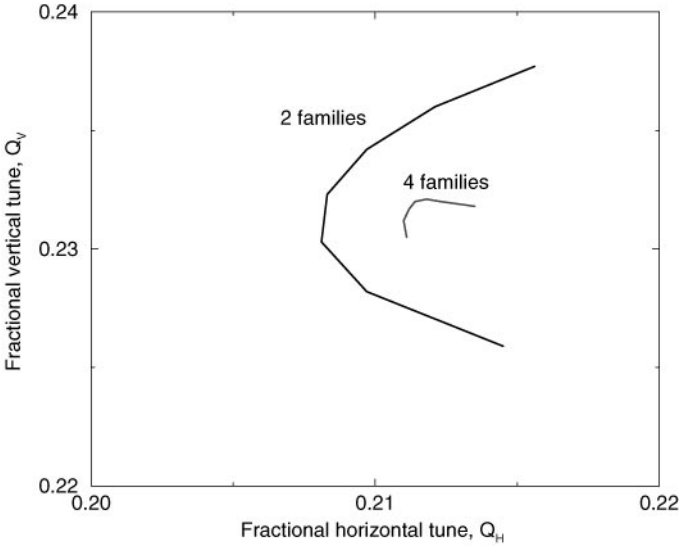

Figure 15 Fractional tune shift as a function of the transition shift, in the range $|\Delta\gamma_T| \leq 0.5$, in a RHIC lattice with $\beta^* = 10$ m at each interaction point. The tune deviations can be reduced even further by fine-tuning the fixed ratios between four families—two *G*-type and two *Q*-type—on the inner and outer RHIC arcs (inner and outer shown in Figure 2).

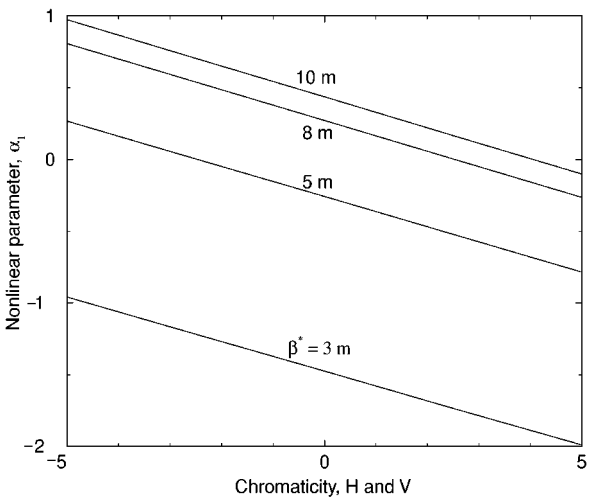

Figure 16 Dependence of the nonlinear parameter α_1 on β^* and on chromaticity (assumed equal in both planes). RHIC passed through transition with $\beta^* = 5$ m during gold ion collisions in 2002.

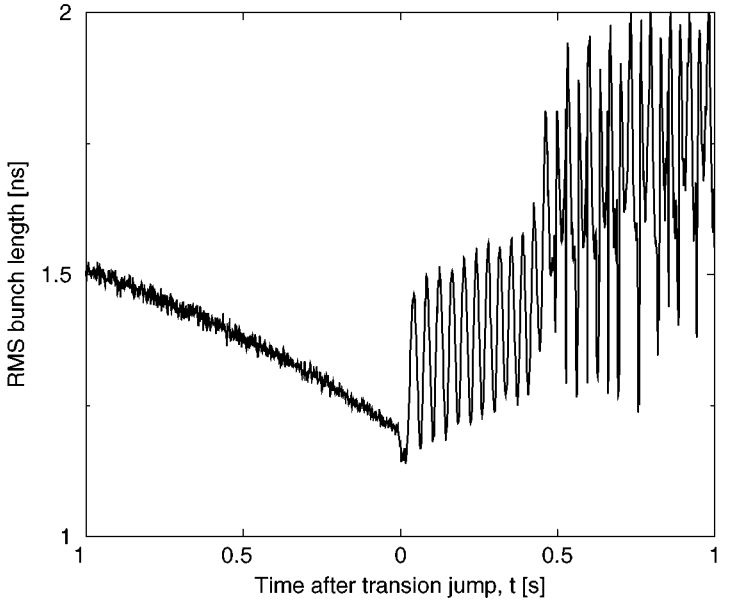

Figure 17 The measured rms bunch length versus time as transition is crossed with high-intensity gold beams. The transition jump occurs at $t = 0$ s, followed by quadrupole oscillations due to an imperfectly matched RF voltage. In this particular ramp, an instability set in at $t = 0.5$ s, leading to significant beam loss.

with $\Delta\gamma_T$ becomes stronger for smaller β^*. A compromise was made in the 2002 RHIC run by passing through transition in a lattice with $\beta^* = 5$ m.

Figure 17 shows the performance of the transition jump with high-intensity gold beams in 2001. The rms bunch length decreased from 1.5 ns to 1.2 ns in the last second as the transition jump was approached with a ramp rate of $d\gamma/dt = 0.5\ \mathrm{s}^{-1}$ (half of the nominal acceleration rate). The transition jump was applied at $t = 0$ s. Quadrupole oscillations were evident immediately after the jump, due to an imperfectly matched RF voltage. In order to suppress head-tail instabilities, the nominal chromaticities were ramped from $\chi = -3$ to $\chi = 2$ as transition was crossed. However, the rate of this chromaticity change was limited by the quench-protection circuitry on the two sextupole families. This slow response is thought to be the root cause of an instability that is sometimes seen after transition with high-intensity beams. Figure 17 shows the instability setting in at about $t = 0.5$ s, eventually leading to significant beam loss. Figure 18 shows the tomographical reconstruction of the longitudinal beam distribution before and after the jump, and after the onset of the instability. The proposed solution to this problem is to install additional fast power supplies on two chromaticity jump sextupoles per arc (J. Kewisch & C. Montag, private communication).

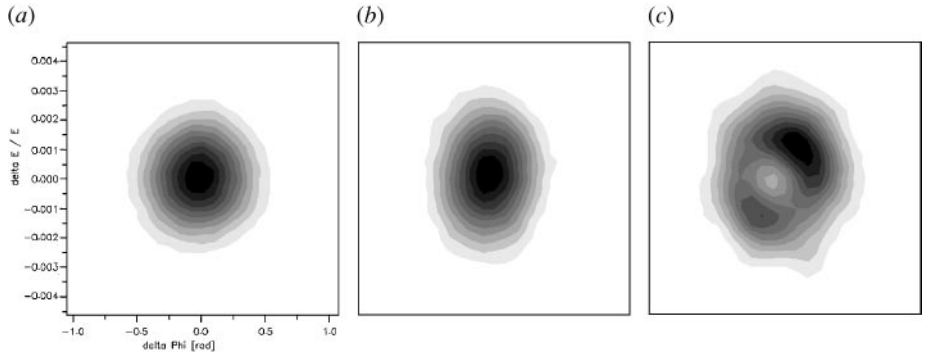

Figure 18 Tomographical reconstruction of the beam distribution in longitudinal phase space. (*a*) Just before the transition jump ($t = -0.5$ s), the distribution is circular. (*b*) Just after the jump ($t = 0.3$ s), an elliptical distortion is visible, indicating a modest RF voltage mismatch. (*c*) After an instability has set in ($t = 0.6$ s), the distribution shows two peaks and a depopulated center.

6. POLARIZED PROTON COLLISIONS AT RHIC

In addition to heavy ion collisions (6), RHIC will also collide intense beams of polarized protons (26), reaching transverse energies at which the protons scatter as beams of polarized quarks and gluons. The study of high-energy polarized proton beams has been a part of the program at Brookhaven, including the development of polarized beams in the Booster and AGS rings for fixed-target experiments. We have extended this capability to the RHIC machine. This section describes the design and methods for achieving collisions of both longitudinally and transversely polarized protons in RHIC at energies up to $\sqrt{s} = 500$ GeV.

6.1. Spin Dynamics and Siberian Snakes

Accelerating polarized beams requires the control of both the orbital motion and spin motion. Whereas the effect of the spin on the orbit is negligible, the effect of the orbit on the spin is usually very strong. The evolution of the spin direction of a beam of polarized protons in external magnetic fields such as those in a circular accelerator is governed by the Thomas-BMT equation (27),

$$\frac{d\vec{P}}{dt} = -\left(\frac{e}{\gamma m}\right)[G\gamma \vec{B}_{\perp} + (1+G)\,\vec{B}_{\parallel}], \times \vec{P}, \qquad 31.$$

where the polarization vector $\vec{P}$ is expressed in the frame that moves with the particle, and $\vec{B}_{\perp}$ and $\vec{B}_{\parallel}$ are the magnetic field components transverse and parallel to the beam direction. This simple precession equation is very similar to the Lorentz force equation, which governs the evolution of the orbital motion in an external

magnetic field:

$$\frac{d\vec{v}}{dt} = -\left(\frac{e}{\gamma m}\right)[\vec{B}_{\perp}] \times \vec{v}. \qquad 32.$$

From a comparison of these two equations, it is readily apparent that, in a pure vertical field, the spin rotates $G\gamma$ times faster than the orbital motion. Here $G = 1.7928$ is the anomalous magnetic moment of the proton and $\gamma = E/m$. In this case, the factor $G\gamma$ then gives the number of full spin precessions for every full revolution, a number that is also called the spin tune $\nu_{\rm sp}$. At the highest RHIC energy (250 GeV), this number reaches 478. The Thomas-BMT equation also shows that at low energies ($\gamma \approx 1$) longitudinal fields ($\vec{B}_{\parallel}$) can be quite effective in manipulating the spin motion, but at high energies transverse fields ($\vec{B}_{\perp}$) are necessary to have any effect beyond the ever-present vertical holding field.

The acceleration of polarized beams in circular accelerators is complicated by the presence of numerous depolarizing resonances. During acceleration, a depolarizing resonance is crossed whenever the spin precession frequency equals the frequency with which spin-perturbing magnetic fields are encountered. The two main types of depolarizing resonances correspond to the possible sources of such fields: imperfection resonances, which are driven by magnet errors and misalignments, and intrinsic resonances, driven by the focusing fields. The strengths of both types of resonances increase with beam energy.

The resonance conditions are usually expressed in terms of the spin tune $\nu_{\rm sp}$. For an ideal planar accelerator, where orbiting particles experience only the vertical guide field, $\nu_{\rm sp} = G\gamma$, as stated above. The resonance condition for depolarizing resonances caused by field imperfections arises when $\nu_{\rm sp} = G\gamma = n$, where n is an integer. Imperfection resonances are therefore separated by only 523 MeV energy steps. The condition for intrinsic resonances is $\nu_{\rm sp} = G\gamma = kP \pm \nu_y$, where k is an integer, ν_y is the vertical betatron tune, and P is the super-periodicity (i.e., the number of identical sections of the accelerator). For example, at the Brookhaven AGS, $P = 12$ and $\nu_y \approx 8.8$.

Close to a spin resonance, the spin tune deviates away from its value of $G\gamma$ of the ideal flat machine. For a resonance with strength r, which is the total spin rotation due to the resonance driving fields, the new spin tune is given by

$$\cos\left(\pi \nu_{sp}\right) = \cos\left(\pi G\gamma\right)\cos\left(\pi r\right).$$

A similar calculation can be done for the effective precession direction or, as it is now often called, the stable spin direction. The stable spin direction describes those polarization components that are repeated in every turn. Note that both the stable spin direction and the spin tune are completely determined by the magnetic structure of the accelerator and the beam energy. The magnitude and sign of the beam polarization, however, depend on the beam polarization at injection and the acceleration process to which the beam is subjected.

The spin tune and stable spin direction calculations apply only to a time-independent static situation or if parameters are changed adiabatically. Far from

the resonance, the stable spin direction coincides with the main vertical magnetic field. Close to the resonance, the stable spin direction is perturbed from the vertical direction by the resonance driving fields. When a polarized beam is accelerated through an isolated resonance at arbitrary speed, the final polarization can be calculated analytically (28) and is given by

$$P_f/P_i = 2e^{-\frac{\pi|r|^2}{2\alpha}} - 1, \qquad 33.$$

where P_i and P_f are the polarizations before and after the resonance crossing, respectively, and α is the change of the spin tune per radian of the orbit angle. When the beam is slowly ($\alpha \ll |r|^2$) accelerated through the resonance, the spin vector will adiabatically follow the stable spin direction, resulting in complete spin flip. However, at a faster acceleration rate, partial depolarization or partial spin flip will occur.

Traditionally, the intrinsic resonances are overcome by using a betatron tune jump, which effectively makes α large, and the imperfection resonances are overcome with the harmonic corrections of the vertical orbit to reduce the resonance strength r (29). Over the past 10 years, new techniques to cross both imperfection and intrinsic resonances adiabatically have been developed. A localized spin rotator or "partial Siberian snake" can make all the imperfection resonance strengths large and cause complete adiabatic spin flip at every imperfection resonance (30). A single vertical RF dipole magnet can create a strong artificial spin resonance by driving large coherent betatron oscillations, overpowering the effect of the intrinsic resonances.

At higher energies, a "full Siberian snake" (31), which rotates the spin by 180° about a horizontal axis, will keep the stable spin direction unperturbed as long as the spin rotation from the Siberian snake is much larger than the spin rotation due to the resonance driving fields. Therefore, the beam polarization is preserved during acceleration. An alternative description of the Siberian snake's effect comes from the observation that the spin tune with the snake is a half integer and energy-independent. Therefore, neither imperfection nor intrinsic resonance conditions can ever be met unless the betatron tune is a half integer.

A local spin rotator can be constructed at lower energies by using a solenoid, or at high energies by using a sequence of interleaved constant-field horizontal and vertical dipole magnets that produce a local orbit distortion. Because the orbit distortion is inversely proportional to the momentum of the particle, such a dipole snake is particularly effective for high-energy accelerators, e.g., energies above 30 GeV.

Figure 19 shows the layout of the Brookhaven accelerator complex, highlighting the components required for polarized beam acceleration.

6.2. Polarized Proton Injector

A new polarized source based on the optically pumped polarized ion source (OPPIS) technique was recently installed at Brookhaven (32). The new source produced

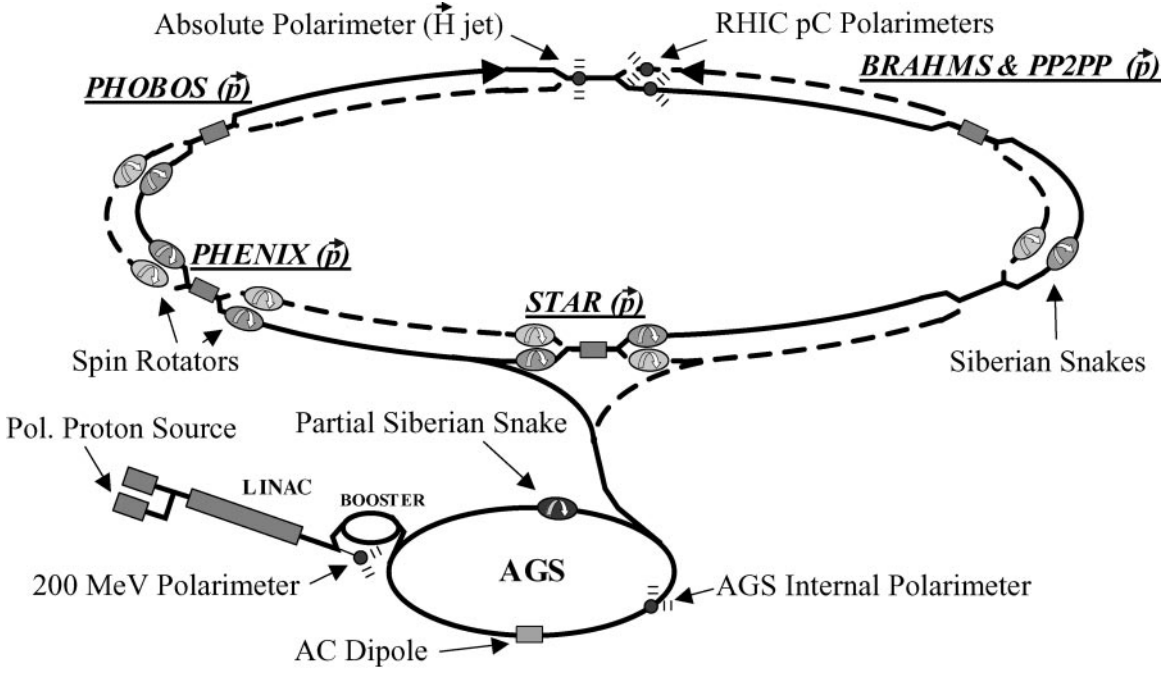

Figure 19 The Brookhaven hadron facility complex, which includes the AGS Booster, the AGS, and RHIC. The RHIC spin project will install two snakes per ring with four spin rotators per detector for helicity-spin experiments.

more than 10^{12} polarized protons per pulse. A single source pulse is captured in a single bunch and accelerated in the Booster and AGS for box-car injection into RHIC. This is ample beam intensity to reach the design value of the bunch intensity of 2×10^{11} polarized protons.

Polarized proton beam experiments at the AGS have demonstrated that a 5% partial snake that rotates the spin by 9° is sufficient to avoid depolarization from imperfection resonances up to the required RHIC transfer energy of about 25 GeV (33). As predicted, the polarization reverses sign whenever $G\gamma$ is equal to an integer. Because the partial snake is a solenoid, it does introduce some orbit coupling, which causes additional weak depolarizing resonances at $G\gamma = n \pm \nu_x$.

It was experimentally verified that strong intrinsic resonances can be overcome by the insertion of an RF dipole magnet (34). Full spin flip can be achieved with a strong artificial RF spin resonance excited coherently for the whole beam by driving large coherent vertical betatron oscillations. The RF dipole was used to completely flip the spin at the four strong intrinsic resonances, $0 + \nu_y$, $12 + \nu_y$, $36 - \nu_y$, and $36 + \nu_y$. During the recent commissioning run, beam polarization of about 40% was maintained at the AGS extraction energy of 25 GeV. Most of the 30% polarization loss during acceleration in the AGS is caused by coupling resonances and weak intrinsic resonances. New betatron tune working points in the AGS should reduce the effect of these weak resonances in the future, and a new AGS partial snake using a helical dipole magnet would eliminate all coupling resonances (35).

At 25 GeV ($G\gamma = 46.5$), the polarized protons are transferred to RHIC. At this energy, the beam transfer line between the AGS and RHIC is spin-transparent (36), avoiding spin rotation from the interleaved horizontal and vertical bends.

With proper care, the normalized emittance of the bunch is expected to be much less than 20π μm. Past tests have achieved vertical beam emittance of $< 10\pi$ μm. The process is repeated until all 120 bunches of each ring are filled. Because each bunch is accelerated independently, the direction of the polarization of each bunch can be prepared independently. Filling each of the two RHIC rings with 120 bunches and accelerating to full energy is a short process ($\sim$10 min) relative to the expected lifetime of the stored polarized proton beams (many hours).

6.3. Polarized Proton Acceleration

To maintain polarization during acceleration, two full Siberian snakes are inserted on opposite sides of the RHIC lattice for each of the two counter-rotating rings. In addition, spin rotators are located on each side of the two major IPs so that the polarization direction can be longitudinal at the collision point. These devices are the primary magnetic components of the polarized beam project at RHIC. Polarimetry instrumentation will also be inserted, as will spin-flip devices to enable manipulation of spin orientation during a store.

6.3.1. SNAKES AND SPIN ROTATORS Each Siberian snake rotates the spin by 180° around a horizontal axis, and the two axes of the two snakes of each ring must be

perpendicular to each other. In RHIC, one snake rotates the spin around an axis that points 45° to the outside of the ring, and the other snake rotates around an axis that points 45° to the inside. In this case, all snakes could be constructed in the same way. The two snakes of each ring must be installed on opposite sides of the ring, with the beam direction in one snake exactly opposite to the beam direction in the other snake to within 0.3 mrad.

Fitting the Siberian snakes and spin rotators into the existing straight sections of RHIC requires a compact design that produces the desired spin rotation in minimal space and with minimal orbit excursions. A particularly elegant solution (37) consists of four helical dipole magnet modules, each having a complete 360° twist. Using helical dipole magnets minimizes orbit excursions, which are most severe at injection energy. This allows for a modular design, in which right-handed superconducting helical dipoles could be used for both snakes and both right- and left-handed helical dipoles are used for the spin rotators near the IPs.

The four snakes and eight rotators require a total of 48 individual full-twist helical dipole magnets with a maximum operating field of 4 T. The four magnets needed to create one snake or one rotator are mounted inside a modified RHIC dipole magnet cryostat. Because it is desirable to independently power the four magnets within the cryostat, the required current was minimized in order to reduce the heat leak due to the power leads. The resulting large inductance can be tolerated because the field strengths of the snake magnets are held constant during the acceleration process. Design and construction of the snakes and rotators are discussed elsewhere (38).

The orbit through an ideal full-twist helical dipole has the incoming and outgoing rays parallel, but transversely displaced. In order to have a net displacement of zero through a snake, the inner pair and outer pair of helical dipoles are powered with opposite fields to cancel this orbit offset. Figure 20 shows the field components, design orbit, and spin rotation through a snake at injection energy. At 250 GeV, the required fields are almost the same, and the orbit displacement in the middle of the snake is only about 3 mm.

By operating the helices at different currents, it is possible to adjust both the amount of spin rotation (angle μ) and axis of rotation. With the helices wired as described above, the axis of rotation for the snake is in the horizontal plane at an angle ϕ from the longitudinal direction. Figure 21 shows the dependence of μ and ϕ on the two field settings—B_1 for the outer pair of helices and B_2 for the inner pair.

The direction of the spin rotator beam line in RHIC is at a horizontal angle $\theta = 3.674$ mrad with the direction of the adjacent insertion, so the spin should emerge from the rotator in the horizontal plane and at an angle $G\gamma\theta$ with the rotator axis in order to obtain a longitudinal polarization through the insertion region. The needed rotation therefore depends on the beam energy. The values of the field needed to provide a longitudinal polarization at different energies are shown in Figure 22. The rotators will be turned on only after the beams are accelerated to the desired storage energy.

All snakes are operated at constant field throughout injection and acceleration. The total twist angle and its tolerance are $360° \pm 2°$(39), and the required field

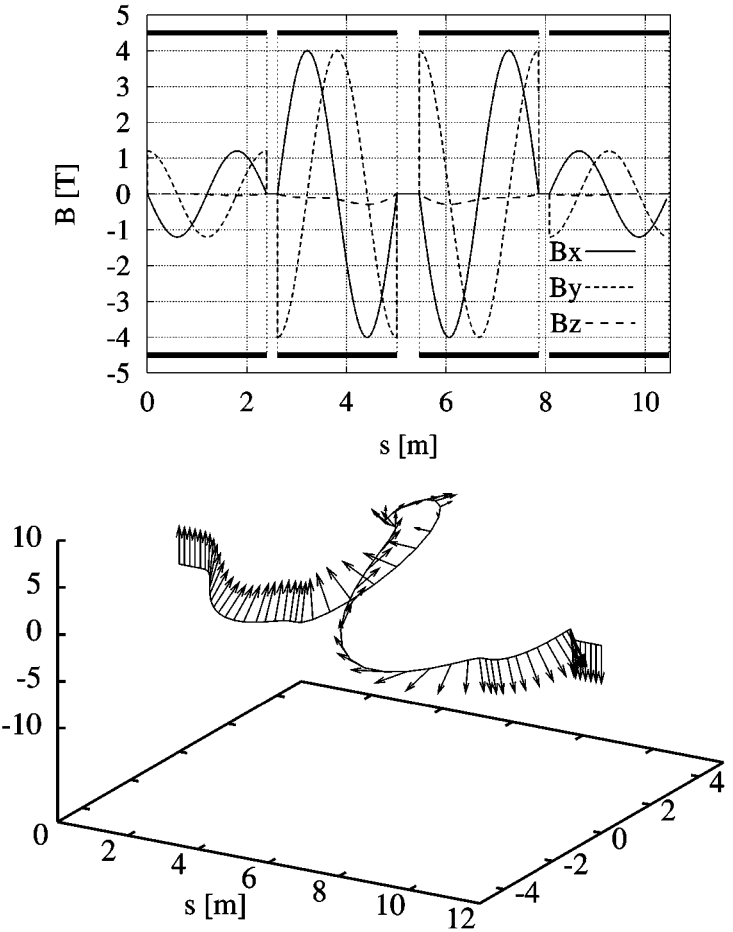

Figure 20 Field, orbit, and spin tracking through the four helical magnets of a Siberian snake at $\gamma = 25$. The spin tracking shows the reversal of the vertical polarization.

integrals, $\int B_x d\ell$ and $\int B_y d\ell$, should be less than 0.05 Tm. Orbit distortions generated by these errors can easily be corrected using standard RHIC dipole correctors. The ends of the magnets have been carefully designed to obtain not only the desired vanishing integrated field strength but also the total field twist well within these tolerances (40, 41).

6.3.2. POLARIZED PROTON ACCELERATION With full snakes, all depolarizing resonances should be avoided, since the spin tune is a half integer independent of energy. However, if the spin disturbance from small horizontal fields is adding up significantly between the snakes, depolarization can still occur. This effect is most

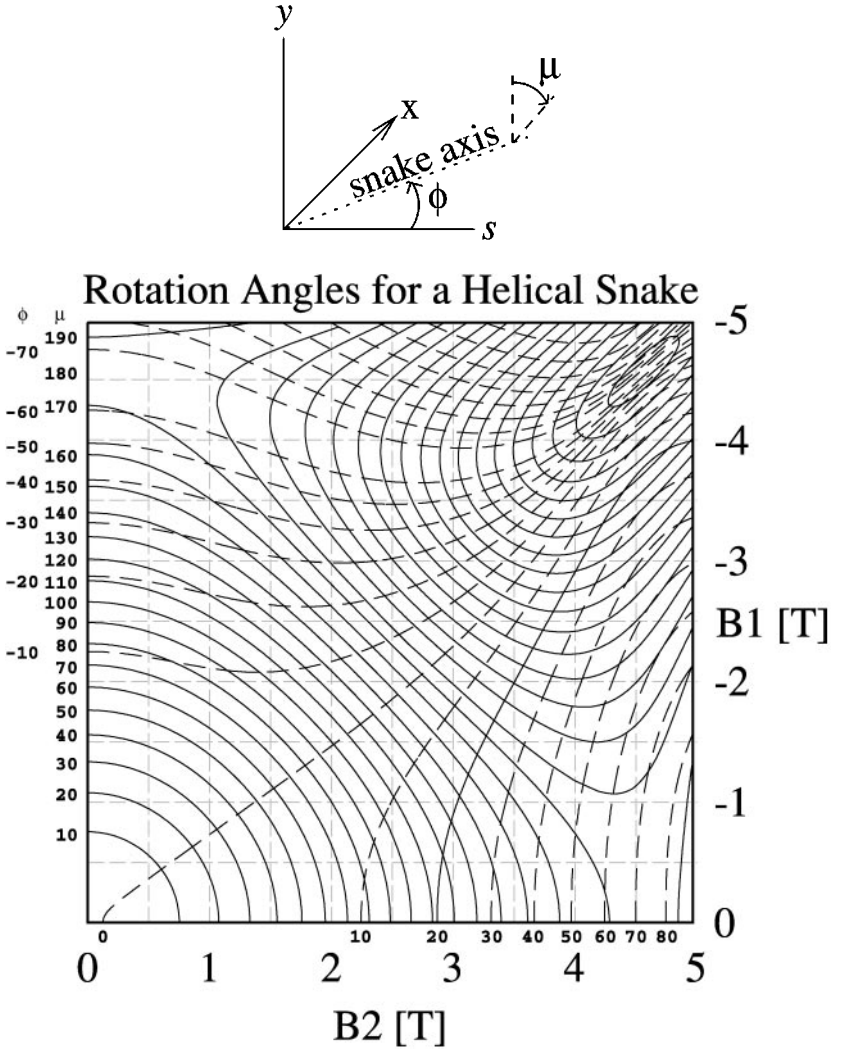

Figure 21 Change of the direction of the snake rotation axis as a function of magnet excitation. This calculation uses a simplified analytical expression for the snake magnetic field. The rotation axis of the snake is ϕ and the rotation angle is μ. B_1 is the field strength of the outer pair of helices, and B_2 is the field strength of the inner pair.

pronounced when the spin rotations from all the focusing fields add up coherently, which is the case at the strongest intrinsic resonances. A simplistic rule of thumb would then suggest that as long as the total spin rotation of all the Siberian snakes is much larger than the total spin rotation per turn caused by the strongest spin resonance, the polarization should be preserved during acceleration. This rule holds

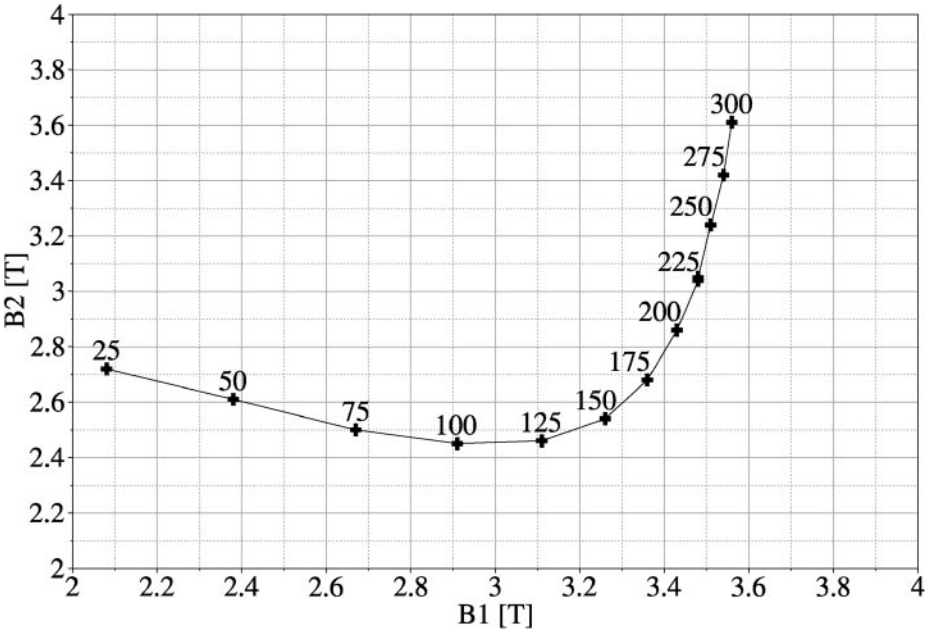

Figure 22 Excitation of the two pairs of helical magnets in the rotator to achieve longitudinal polarization in the insertion of RHIC, for various beam energies in GeV.

for the AGS partial Siberian snake with regard to the imperfection resonances. It also predicts that RHIC will need at least two snakes for a beam with a normalized 95% emittance of 20π μm.

The strengths of the intrinsic resonances in RHIC can be calculated quite accurately from the appropriate integral over the horizontal focusing fields. Figure 23 shows the result for the RHIC lattice with $\beta^* = 10$ m at all intersections. A calculation with $\beta^* = 1$ m gave only a slightly different result. The calculation was performed for a particle with a normalized Courant-Snyder invariant of $\varepsilon_0 = 10\pi$ μm. For a different value of the invariant, the strength scales according to

$$r = r_0\sqrt{\frac{\varepsilon}{\varepsilon_0}}, \qquad 34.$$

where r_0 is the resonance strength for the invariant ε_0.

Important intrinsic spin resonances are located at

$$G\gamma = kP \pm \nu_y \approx mPM \pm \nu_B, \qquad 35.$$

where k and m are integers, P is the super-periodicity of the accelerator, M is the number of FODO cells per super-period, and $2\pi\nu_B = 2\pi(\nu_y - 12)$ is the

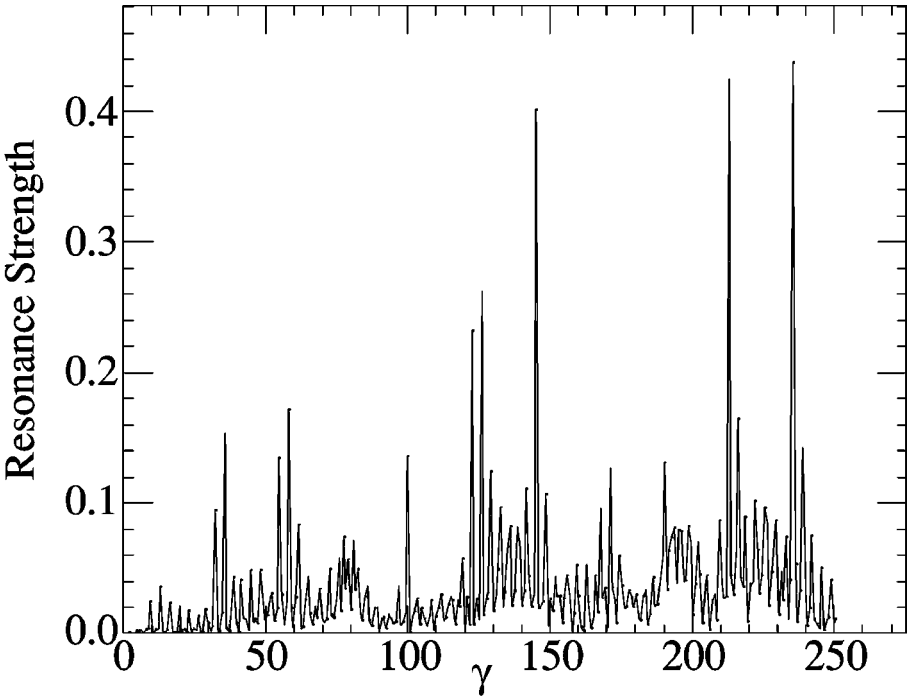

Figure 23 Strengths of the intrinsic depolarizing resonances in RHIC, with $\epsilon_0 = 10\pi\ \mu$m.

accumulated phase advance of all FODO cells, which contain bending dipoles. The strengths of all intrinsic resonances are less than 0.5.

Important imperfection resonances are located at integers closest to strong intrinsic resonances if the closed orbit is not corrected. Figure 24 shows the imperfection resonance strengths obtained from an initial random sample of magnet misalignments with a rms spread of ± 0.5 mm, dipole roll angles with a spread of ± 1 mrad, dipole field errors of $\pm 5 \times 10^{-4}$, and position monitor errors of ± 0.5 mm, after a vertical closed orbit correction to within 0.155 mm rms. The strengths of the imperfection resonances then generally increase linearly with the beam energy and are bounded by

$$r_{\text{imp}} = 0.25\,\frac{\gamma}{250}\,\sigma_y\ (\text{mm}), \qquad 36.$$

where σ_y is the rms value of the residual closed orbit excursions in millimeters. For $\sigma_y = 0.15$ mm, the imperfection resonance strengths are smaller than 0.04 at all energies. Present alignment data show beam position, monitor, and quadrupole placement errors each well below 0.5 mm. The dipole roll angle is also well below 0.5 mrad (43).

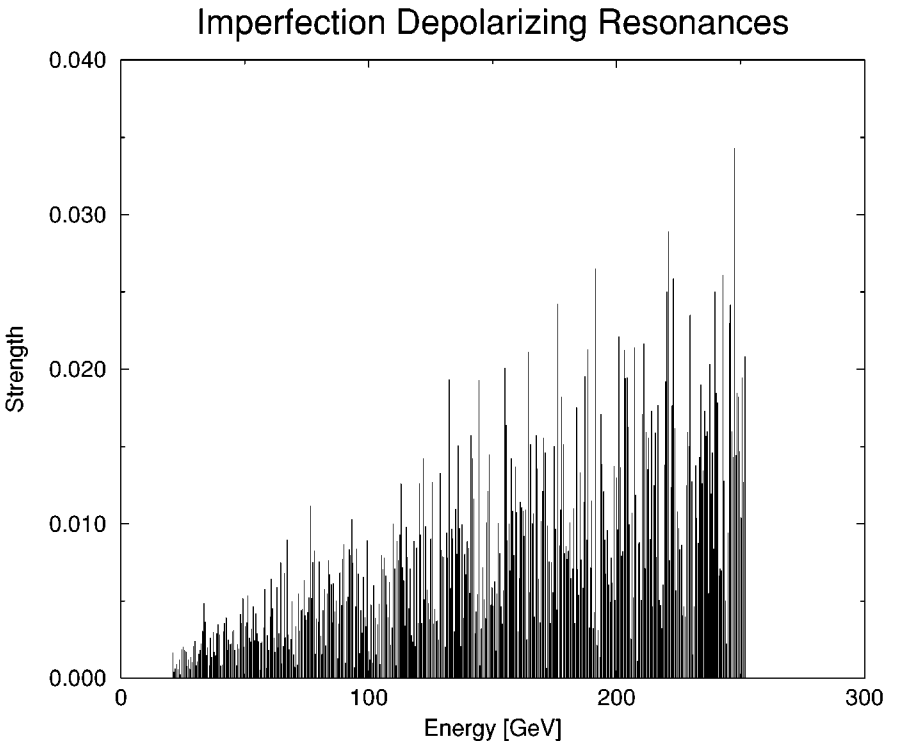

Figure 24 Strengths of the imperfection depolarizing resonances in RHIC calculated after MICADO (42) orbit correction for orbit error of <150 μm, $\beta^* = 10$ m.

In the presence of strong depolarizing resonances, depolarization can result from resonance conditions extending over more than just one turn. This leads to additional possible depolarizing resonance conditions:

$$\Delta\nu_y = \frac{\nu_{\rm sp} \pm k}{n}. \qquad 37.$$

These are called snake resonances (44), and n, the number of turns, is called the snake resonance order. For two snakes, depolarization from snake resonances becomes significant only at an intrinsic resonance strength of about 0.5, and even-order snake resonances additionally require an imperfection resonance strength of about 0.05. Figure 25 shows the result of a simple one-dimensional spin tracking calculation through an energy region (using the RHIC acceleration rate) with an intrinsic resonance strength of 0.5 and an imperfection resonance strength of 0.05. Some regions of the betatron tune in RHIC experience no depolarization. With the betatron tune and its spread located between 0.220 and 0.235, well separated from the snake resonances $1/4 = 0.25$ and $3/14 = 0.2143$, no depolarization will occur over the whole RHIC energy range.

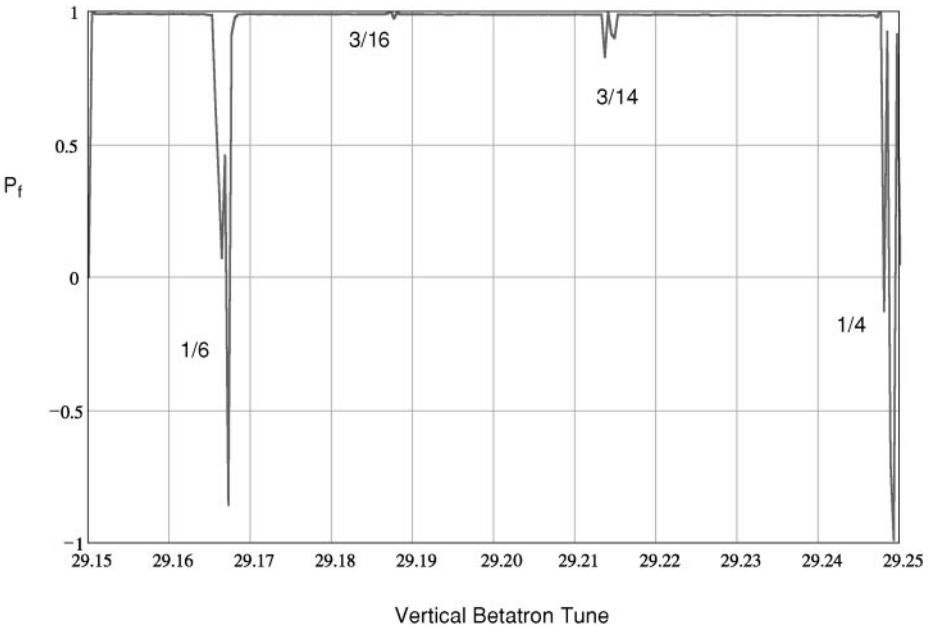

Figure 25 Vertical component of the polarization after acceleration through a strong intrinsic resonance and a moderate imperfection resonance, shown as a function of the vertical betatron tune for two snakes, a spin tune of 0.5, an intrinsic resonance strength of 0.5, and an imperfection resonance strength of 0.05.

Extensive spin tracking also confirms that two Siberian snakes, a well-corrected closed orbit, and a well-controlled betatron tune should ensure no loss of polarization up to the top energy of 250 GeV. The acceleration through the energy region of the strongest resonance was simulated in great detail, including a 1-mm rms misalignment of the quadrupoles and sextupoles. The corrector dipoles used to correct the closed orbit were also included in the spin tracking. The result is shown in Figure 26 for a beam with a normalized 95% emittance of 20π μm. Despite a significant decrease of the polarization at the energy of the resonance at $G\gamma = 5 \times 81 + (\nu_y - 12) = 422.18$, the polarization of the full beam is restored after it accelerates completely through the resonance region. The simulation also shows significant polarization loss at the edge of the beam, which highlights the need for a polarimeter that can measure polarization profiles.

6.3.3. SPIN REVERSAL OF STORED BEAMS Because of the high precision of the proposed asymmetry measurements, frequent polarization sign reversal is imperative to avoid systematic errors arising from luminosity variations, crossing-angle variations, and detector-efficiency variations. As mentioned above, different bunches will have different polarization signs, and therefore different bunch crossings will measure interactions with different combinations of incoming beam polarizations. Although this will greatly reduce systematic errors, it is still true that

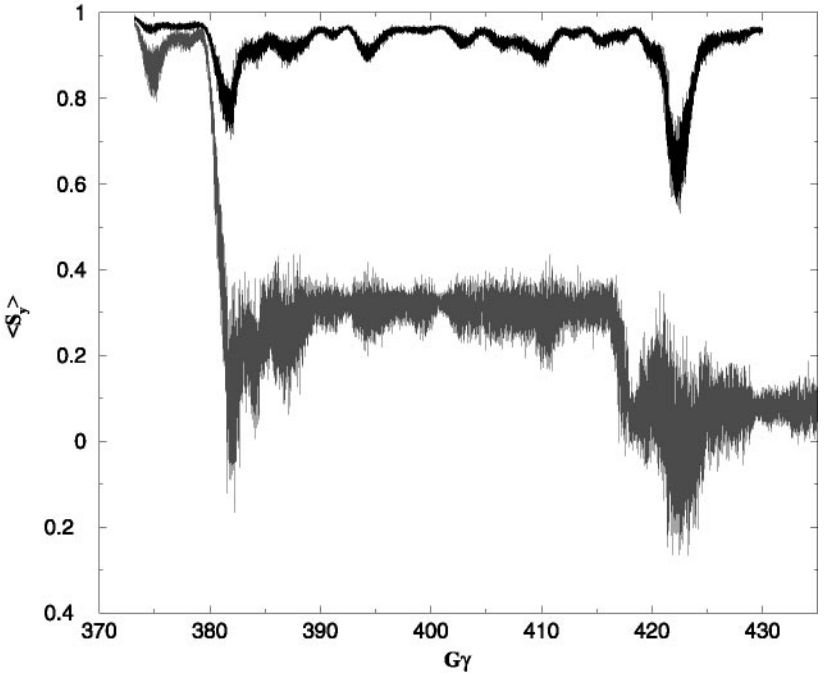

Figure 26 Result of spin tracking through the region of the strongest resonance in RHIC. The closed orbit was corrected with residuals of less than 0.2 mm. The upper and lower curves show the result for the full beam and the particles at the edge of the beam, respectively.

one pair of bunches will always cross with the same combination of polarization signs during the whole beam store, which is at least several hours. The possibility of systematic errors is eliminated by the installation of a spin flipper, which reverses the polarization sign of all bunches. The spin flipper consists of a vertical dipole magnet excited by about 40 kHz AC current. This magnet will drive an artificial spin resonance, which can be used to adiabatically reverse the polarization direction. High-efficiency spin reversal in the presence of a solenoidal Siberian snake has recently been demonstrated at the low-energy cooler ring at the Indiana University Cyclotron Facility (IUCF) (45). We estimate that complete spin reversal would take less than 1 s. The same device will accurately measure and adjust the spin tune by measuring the spin reversal efficiency as a function of the frequency of the spin flipper excitation.

To avoid emittance growth from the oscillating vertical deflections, the dipole needs to be turned on and off slowly (adiabatically), as shown in Figure 27. This scheme was successfully tested in the AGS, where adiabatic build-up of betatron oscillation amplitudes in excess of two beam sigma, and subsequent adiabatic de-excitation, were demonstrated without emittance growth (46).

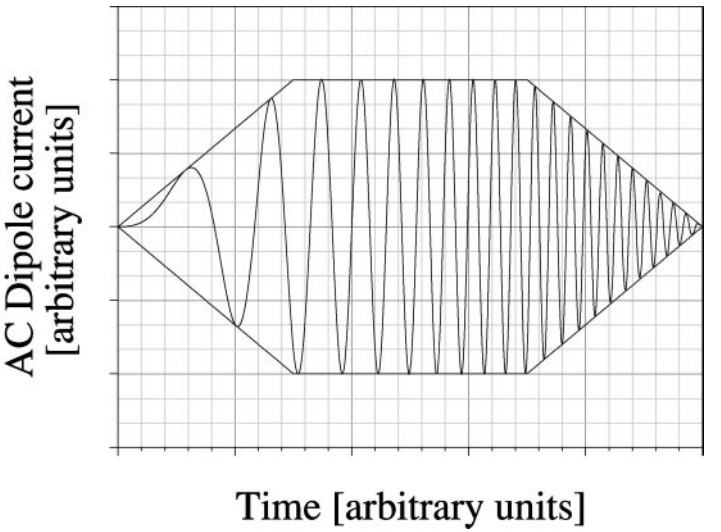

Figure 27 Schematic diagram of the excitation dipole current as a function of time. Note the increase of frequency with time. The trapezoidal lines are the amplitude envelopes.

6.4. Measuring Beam Polarization

Successful commissioning of polarized beam acceleration and storage requires both relative and absolute polarimetry. Relative polarization measurements may use a spin-sensitive process that has a high rate but is uncalibrated. The fast relative polarimeters in RHIC are based on the asymmetry in proton-carbon (pC) elastic scattering in the Coulomb-nuclear interference (CNI) region. It is expected that the relative beam polarization for each measurement can be determined by using a polarimeter to pC CNI 10% in <1 min at full luminosity. The future addition of polarized proton jet target will allow the calibration of the pC CNI polarimeter to better than 5%.

Vertical beam polarization is measured by determining the asymmetry in the cross section for left and right scattering or particle production, using a reaction with a known analyzing power A_p:

$$P_B = \frac{1}{A_p}\frac{N_L - N_R}{N_L + N_R}. \qquad 38.$$

P_B is the beam polarization; N_L and N_R are the numbers of particles that scatter to the left and right (respectively) normalized by luminosity. A_p can be known from experiment or theory.

Small-angle elastic scattering of hadrons in the CNI region has long been advocated for polarimetry. The predicted asymmetry is significant and largely independent of energy above a few GeV. Assuming negligible contribution from hadronic spin flip, elastic scattering in the small-angle CNI region is predicted to have a

calculable analyzing power of about 3%–5%, as well as a large cross section over the whole RHIC energy range from 24 GeV/c to 250 GeV/c (47). The analyzing power is given by

$$A_p(t) = \frac{G t_0 t \sqrt{t}}{m_p(t^2 + t_0^2)}, \qquad 39.$$

where G is the anomalous magnetic moment of the proton (1.7928), m_p the proton mass, and $t_0 = \frac{8\pi\alpha Z}{\sigma_{\text{tot}}}$. The total cross section σ_{tot} is only weakly energy-dependent over the relevant energy range. Figure 28 shows the calculated analyzing power for a hydrogen target ($Z = 1$, $\sigma_{\text{tot}} = 35$ mb) and a carbon target [$Z = 6$, $\sigma_{\text{tot}} = 330$ mb (48)] as a function of $(-t)$.

A calibration of the analyzing power of the pC CNI process with proton-proton elastic scattering at 23 GeV gave an effective value for the RHIC polarimeter at injection energy of about 0.012 (49). Even this low value, along with the very high cross section, gives a very large figure of merit (NA_p^2). At high energy with typical values of $-t$ from 0.002 to 0.01 GeV^2, scattering results in both a very small forward angle of the scattered proton and a very low kinetic energy of the carbon recoil (0.1–1 MeV). Because it is impractical to measure the forward-scattered

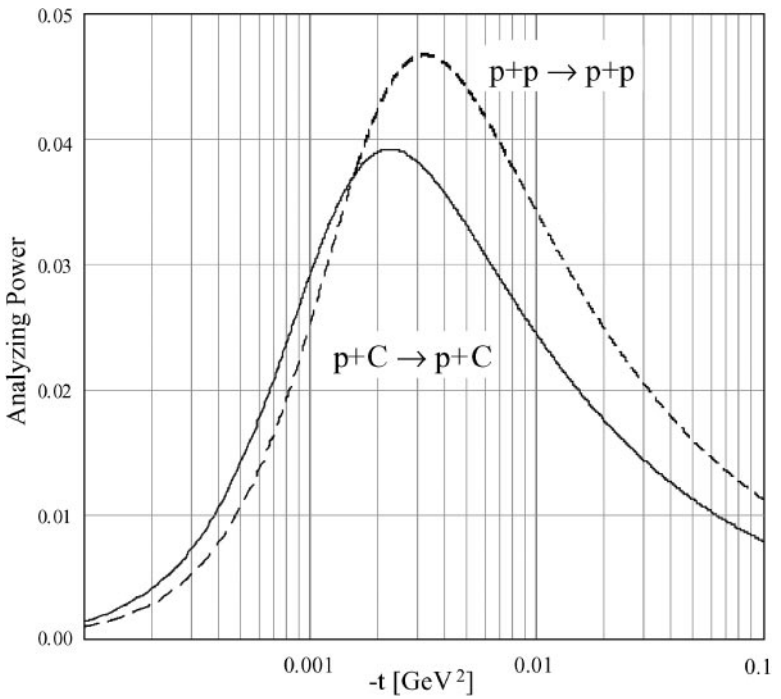

Figure 28 Coulomb-nuclear interference analyzing power for pp and pC scattering as a function of the momentum transfer $-t$.

proton, it is necessary to rely solely on the measurement of the recoil carbon nuclei to identify elastic scattering. The ultra-thin ribbon carbon targets developed at IUCF are ideal for the *p*C CNI polarimeter, both to survive in the RHIC beam and to get the carbon nuclei out of the target in the CNI region, where the kinetic energy of the recoil carbon is only hundreds of keV. The detectors are placed so that the carbon arrives between the passage of beam bunches, thus avoiding any prompt background. The polarimeters are located near Q4 in section 12, where the vertical and horizontal beta functions are small, thus reducing the effect of multiple scattering on emittance dilution.

Manipulating polarization in RHIC requires information on both vertical and horizontal components of beam polarization. In addition to one pair of detectors in the horizontal plane, two pairs of detectors at $\pm 45^\circ$ are added, which measure both transverse components (see Figure 29). When these two pairs are used to measure either vertical or radial polarization components, the analyzing power is reduced by a factor of $\cos 45^\circ = 1/\sqrt{2}$.

6.5. First Polarized Proton Run

The first polarized proton run in RHIC took place from December 2001 to January 2002 (50). Polarized beam was successfully accelerated to 100 GeV and stored and collided with a peak luminosity of about 1.5×10^{30} cm^{-2} s^{-1}. The beam polarization at the AGS was only about 30%, mainly because it was necessary to use a back-up AGS main power supply with a much reduced ramp rate that amplified the strength of the depolarizing resonances. However, essentially all beam polarization was preserved during acceleration and beam storage. Figure 30 shows circulating beam current and measured asymmetries of two typical stores. The analyzing power at 100 GeV for the RHIC polarimeters is not known but is expected to be similar to the value at injection energy. Under this assumption,

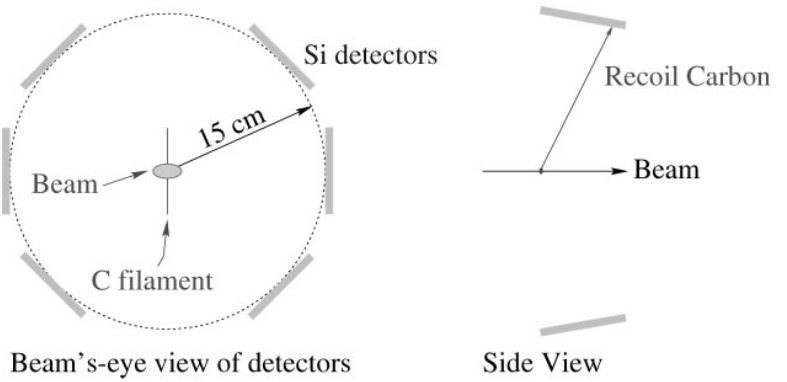

Figure 29 Cross section of the target chamber. Beam is going into the paper and hits the carbon target in the center of the beam pipe. The carbon target is 5.5 μg/cm^2 thick and 11.6 μm wide.

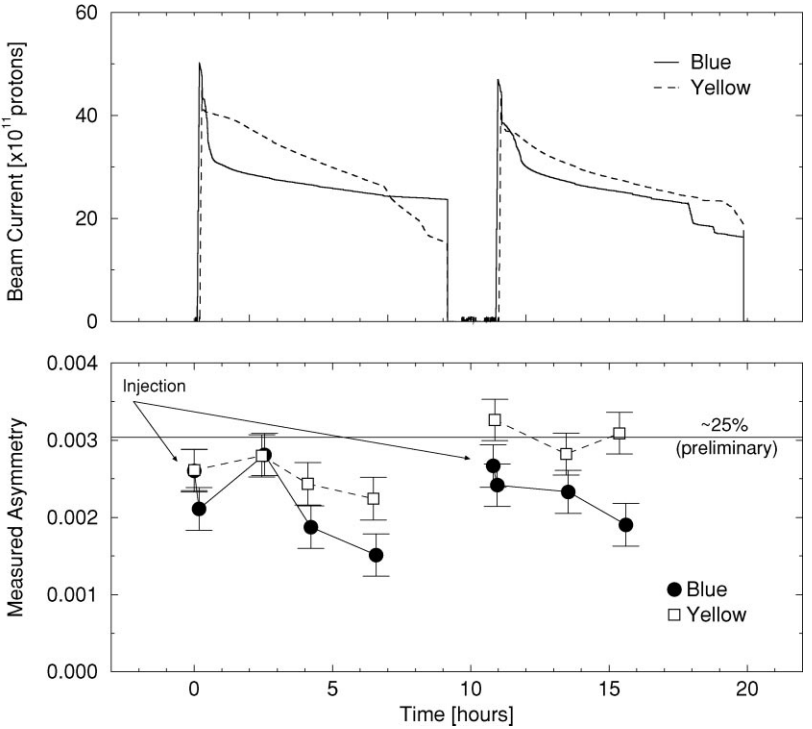

Figure 30 Circulating beam and measure asymmetry in the Blue and Yellow RHIC ring for two typical polarized proton stores.

the polarization at store was typically about 25%. To preserve beam polarization during acceleration and storage, the vertical betatron tune had to be maintained between 0.220 and 0.235, and the orbit had to be corrected to better than 1 mm rms. This is in good agreement with the predictions from spin tracking calculations described above.

7. CONCLUSIONS

The initial operation of the RHIC facility has been very successful. The nominal design luminosity of 2×10^{26} cm^{-2} s^{-1} was achieved during the first two physics running periods with gold ions. Almost all of the nominal technical parameters of this unique facility have been realized, opening up frontiers for research in many areas of physics.

The longitudinal phase-space evolution during stores is consistent with intrabeam scattering (IBS) estimates. The transverse phase space is growing faster than would be expected purely from IBS, indicating additional heating mechanisms. This has resulted in a somewhat shorter luminosity lifetime than nominal.

The machine optics with the injection lattice is close to design, though some mismatch is apparent during collisions when the IRs are operating at maximum focusing strength. Coupling in the final-focus quadrupoles is also larger than expected, though still within the capabilities of the correction systems. Operation with multiple identical particle species has proven straightforward, as expected; the much more demanding collisions between different species are anticipated in the next running period. Transition crossing with the γ_T jump works well with minimal emittance growth, beam loss, and tune variation. Problems with transition crossing are related to the fact that reversing chromaticity during the jump has proved too slow to prevent beam instability. Power-supply modifications to provide a more rapid chromaticity jump are in progress. The first highly demanding run with polarized proton collisions was very encouraging. In RHIC with full Siberian snakes, there was no obvious loss of polarization during the ramp, and the polarization lifetime was good during the store. The design goal of 70% polarization at high luminosity still appears realistic.

The future evolution of RHIC depends fundamentally on combatting IBS. The proposed RHIC II upgrade directly compensates for IBS with a high-energy (50 MeV) electron cooling system that would significantly increase the average luminosity. In the interim, luminosity will be further enhanced by an increased number of bunches, higher bunch populations, and reduced β^* values.

ACKNOWLEDGMENTS

The authors wish to acknowledge the assistance of Gerry Bunce, Wolfram Fischer, Haixin Huang, Jorg Kewisch, Waldo Mackay, Christoph Montag, and Erich Willen during the preparation of this article. We would also like to acknowledge the many members of the Brookhaven National Laboratory team that designed, fabricated, commissioned, and operated RHIC.

The *Annual Review of Nuclear and Particle Science* is online at http://nucl.annualreviews.org

LITERATURE CITED

1. Bjorken J, Mtingwa S. *Part. Accel.* 13:115 (1983)
2. Piwinski A. *CERN Accel. School*, p. 405. Geneva: CERN (1984)
3. Wei J. *Part. Accel. Conf.*, p. 3561 (1993) Washington, DC: IEEE/APS
4. Cameron PR, et al. *Part. Accel. Conf.* New York: IEEE/APS (1999)
5. Fischer W, et. al. *Part. Accel. Conf.* (2001) Chicago: IEEE/APS
6. Hahn H, ed. *RHIC Design Manual*. http://www.rhichome.bnl.gov/NT-share/rhicdm
7. Peggs S. *Protons on gold at identical rigidities*. *RHIC/AP/134*, Brookhaven Natl. Lab. (1997)
8. Peggs S. *LHC beam-beam workshop. CERN-SL-99-039 AP*, p. 70; *RHIC/AP/169*, Brookhaven Natl. Lab. (1999)
9. Siergiej D. *Beam-beam interaction effects in the Fermilab collider.* PhD thesis. Univ. New Mexico (1995)

10. Lee SY, Wei J. *Eur. Part. Accel. Conf.*, p. 764 (1988) Rome: World Sci.
11. Wei J. *Longitudinal dynamics of the non-adiabatic regime of alternating-gradient synchrotrons.* PhD thesis. State Univ. NY Stony Brook (1990)
12. Wei J. *AD/RHIC-84*, Brookhaven Natl. Lab. (1991)
13. Wei J. *Eur. Part. Accel. Conf.* (1992) Berlin: World Sci.
14. Tang C. *Some topics in physics—PP2PP, DFT revisited, and transition crossing in RHIC.* PhD thesis. State Univ. NY Stony Brook (2001)
15. Peggs S, Tepikian S, Trbojevic D. *Part. Accel. Conf.* (1993) Washington, DC: IEEE/APS
16. Kewisch J, Tang C. *C-A/AP/53*, Brookhaven Natl. Lab. (2001)
17. Sorenssen A. *Part. Accel.* 6:141 (1975)
18. Johnsen K. *CERN Symp. High Energy Accel. and Pion Phys.* 1:106 (1956)
19. Takayama K. *Part. Accel.* 14:201 (1984)
20. Risselada T. *CERN PS/90-51* CERN (1990)
21. Hardt W, Schonauer H, Sorenssen A. *Int. Conf. High Energy Accel.* Geneva: CERN (1971)
22. Merz W, Ankenbrandt C, Koepke K. *Part. Accel. Conf.* p. 1343 (1987) Washington, DC: IEEE/APS
23. Peggs S, Bogacz SA, Harfoush F. *Part. Accel. Conf.* p. 1660 (1991) San Francisco: IEEE/APS
24. Mi J. *Part. Accel. Conf.* p. 1279 (2001) Chicago: IEEE/APS
25. Bogacz SA, Peggs S. *Part. Accel. Conf.* p. 1657 (1991) San Francisco: IEEE/APS
26. Alekseev I, et al. http://www.agsrhic home.bnl.gov/RHIC/Spin/design (1998)
27. Thomas LH. *Phil. Mag.* 3:1 (1927) Bargmann W, Michel L, Telegdi VL. *Phys. Rev. Lett.* 2:435 (1959)
28. Froissart M, Stora R. *Nucl. Instrum. Methods* 1:297 (1960)
29. Khoe T, et al. *Part. Accel.* 6:213 (1975); Laclare JL, et al. *J. Phys. (Paris), Colloq.* 46:499 (1985); Sato H, et al. *Nucl. Instrum Methods A* 272:617 (1988); Khiari FZ, et al. *Phys. Rev. D* 39:45 (1989)
30. Roser T. *AIP Conf. Proc.*, ed. KJ Heller, 187:1442. New York: AIP (1988)
31. Derbenev YaS, et al. *Part. Accel.* 8:115 (1978)
32. Zelenski AN, et al. *Part. Accel. Conf.* p. 106 New York: IEEE (1999)
33. Huang H, et al. *Phys. Rev. Lett.* 73:2982 (1994)
34. Bai M, et al. *Phys. Rev. Lett.* 80:4673 (1998)
35. Roser T, et al. *AGS/RHIC/SN-072*, Brookhaven Natl. Lab. (1998)
36. Lee SY, Courant E. *AD/RHIC-63*, Brookhaven Natl. Lab. (1990)
37. Ptitsin VI, Shatunov YuM. *Nucl. Instrum. Methods A* 398:126 (1997)
38. MacKay WW, et al. *DESY-PROC-1999-03* p. 163
39. Syphers MJ. *AGS/RHIC/SN-058*, Brookhaven Natl. Lab. (1997)
40. Okamura M. *AGS/RHIC/SN-061*, Brookhaven Natl. Lab. (1997)
41. Jain AK. *AGS/RHIC/SN-062*, A334:173 Brookhaven Natl. Lab. (1993)
42. Autin B, Marti Y. *CERN/ISR-MA/73-17* (1973)
43. Wei J. *RHIC/AP/117*, Brookhaven Natl. Lab. (1996)
44. Lee SY, Tepikian S. *Phys. Rev. Lett.* 56:1635 (1986)
45. Blinov BB, et al. *Phys. Rev. Lett.* 88:14801 (2002)
46. Bai M, et al. *Phys. Rev. E* 56:6002 (1997)
47. Buttimore NH, et al. *Phys. Rev. D* 18:694 (1978); Buttimore NH. *AIP Conf. Proc.* 95:634. New York: AIP (1983)
48. Rosen JL. *AIP Conf. Proc.* 26:287. New York: AIP (1975)
49. Tojo J, et al. *Phys. Rev. Lett.* 89:52302 (2002)
50. MacKay W, et al. *European Part. Accel. Conf.* (2002) Paris: World Sci.

Annual Review of Nuclear and Particle Science
Volume 52, 2002

CONTENTS